

Nanocrystalline Li–Al–Mn–Si Foil as Reversible Li Host: Electronic Percolation and Electrochemical Cycling Stability

Huimin Fan,^{†,‡,⊥} Bo Chen,^{†,§,⊥} Sa Li,^{*,†,‡} Yue Yu,^{†,‡} Hui Xu,^{†,‡} Mengwen Jiang,^{†,‡} Yunhui Huang,^{†,‡} and Ju Li^{*,§,⊥}

[†]School of Materials Science and Engineering, Tongji University, Shanghai 201804, China

[‡]Institute of New Energy for Vehicles, Tongji University, Shanghai 201804, China

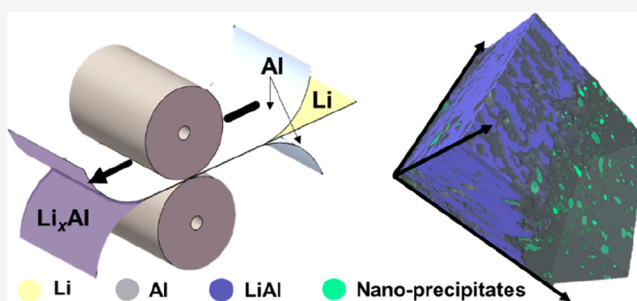
[§]Department of Nuclear Science and Engineering and Department of Materials Science and Engineering, Massachusetts Institute of Technology, Cambridge, Massachusetts 02139, United States

[⊥]Key Laboratory of Performance Evolution and Control for Engineering Structures of Ministry of Education, Tongji University, 1239 Siping Road, Shanghai 200092, China

Supporting Information

ABSTRACT: When a metallic foil (Li metal or Li_xAl) with initial Li inventory (LiInv) is used as the anode in lithium-ion batteries, its metallurgical damage state in the presence of organic liquid electrolyte and cycling electrochemical potential is of great interest. While Li_xAl foil operates at a voltage that eliminates Li_{BCC} dendrite, the state-of-health (SOH) of Li_xAl anode can still degrade quickly in full-cell cycling. To analyze the causes, we decompose $\text{SOH} = \text{SOHe} \times \text{SOHi} \times \text{LiInv}$, where SOHe is SOH of electronic percolation within the anode, SOHi is SOH of Li percolation from cathode to the anode interior, and LiInv is the amount of cyclable lithium in a full cell, all normalized such that 1 means perfectly healthy, and 0 means dead. Any of the three (SOHe, SOHi, LiInv) dropping to zero would mean death of the full cell. Considering the poor performance of pure Al foil due to rapid drop in LiInv, we employed a mechanical prelithiation (MP) method to make LiInv >1 initially. The chemomechanical shock from MP creates an ultrananocrystalline LiAl layer with grain size 10–30 nm on top of unreacted Al. We then monitor SOHe evolution of the anode foil by measuring the in-plane electronic conductance *in situ*. We find that small additions of Mn or Si into Al induce nanoprecipitates Zener pinning, and the resulting denser grain boundary (GB) network before MP significantly reduces foil porosity after MP, delays gross foil fracture, and improves SOHe in subsequent cycling. Microstructural analysis reveals that the refined grain size of foil before MP relieves stress and reduces the chance of forming electronically isolated dead grain cluster due to cracking and invasion of electrolyte and solid–electrolyte interphase (SEI). By maintaining good electronic percolation, binder-free Li_xAlMnSi anode demonstrates an order-of-magnitude more stable SOHe and better electrochemical cycling performance than Li_xAl anode.

KEYWORDS: Nanoprecipitates, prelithiation, chemomechanical shock, ultrananocrystalline, porosity, lithiation/delithiation ductility



Aluminum may be a competitive anode candidate for lithium-ion batteries (LIBs), given its low cost,¹ high theoretical capacity (993 mAh g⁻¹ for LiAl),² and moderate electrochemical potential that inhibits the formation of Li_{BCC} dendrites even at high rates. Dense free-standing Li_xAl foil, as a variation of the popular pure Li_{BCC} metal foil with starting lithium inventory (LiInv), attracts our attention considering its excellent electronic conductivity and dendrite-free deposition.^{3,4} Previous attempts at utilizing Al foil anode demonstrated a rapid drop in LiInv due to cumulative Coulombic inefficiency (CI \equiv 1-CE) losses.⁵ To counter this problem, metallurgical prelithiation (MP) of pristine Al foil at room temperature has been proven to be effective.⁶ Because Li_xAl foil is less reactive toward electrolyte and air,⁷ which is hugely advantageous for industrial processing, the free-standing Li_xAl

foil is quite competitive in terms of large-scale production, and such MP method is more efficient than the previous expensive and complicated electrochemical prelithiation^{8,9} and external chemical lithiation paradigms.^{10–12}

Yet, despite the initially enhanced LiInv, SOH of Li_xAl anode still degrades in full-cell cycling. When drastic phase transformation occurs from $\text{Al}_{\text{FCC}} \leftrightarrow \text{LiAl}_{\text{Cubic}}$ with volume change up to $\sim 100\%$, it is a *bona fide* “chemomechanical shock”¹³ and would render much change of the original foil structure. Since grain boundaries (GBs) support faster diffusion than the bulk,^{14,15} the initial invasion of Li always

Received: September 2, 2019

Revised: November 27, 2019

Published: December 17, 2019

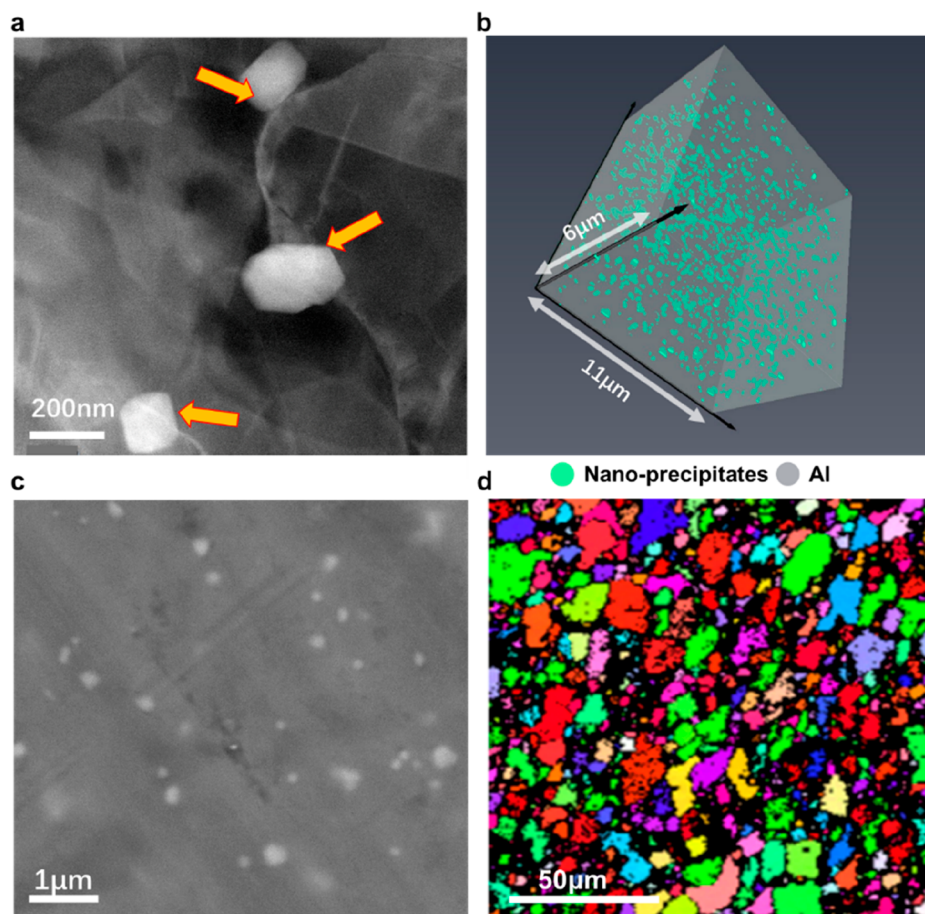
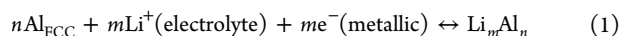


Figure 1. Characterization of AlMnSi foil. (a) TEM characterization of second-phase nanoparticles. (b) FIB-SEM serial-sectioning 3D reconstruction of AlMnSi foil. (c) BSE image of AlMnSi foil. (d) EBSD image of the grain size of AlMnSi foil (contrast with pure Al foil before MP in Figure S1f).

goes along the GB,¹⁶ inducing phase transformations along the way. This imposes a challenge for original grain-to-grain compatibility, making GB sliding and even cracking¹⁷ the main mechanism to accommodate drastic deformation and geometric incompatibility. As local GB sliding is unavoidable, the GB free-volume and GB “complexion”¹⁸ that govern further electronic and mass transport will change. Fundamentally, for the half-cell reaction



to proceed in later battery cycling, global Li^+ ionic (electrolyte) and electronic (metallic) transport must be guaranteed; otherwise, a grain cannot stay electrochemically active. Unlike in the slurry coating case, we do not have explicit binders or conductive agents, so GBs effectively play the role of conductive binders¹⁹ that mechanically hold adjacent grains together and allow electrons to hop across. Generally speaking, the GB “electrochemical complexion” could change in the following gradations during battery cycling: (a) with GB sliding there can be more free volume and accelerated Li atomic diffusivity, a little liquid electrolyte can seep in, forming patches of SEI, but still thin enough that electron can tunnel across, in which case the local electronic conductivity degrades but is still nonzero, (b) a big enough divide has opened up with lots of electrolyte inflow, so that electron tunneling is no longer possible and this GB is no longer conductive electronically, and ultimately (c) all the grain boundaries

surrounding one grain or cluster of grains have achieved (b) status, so this grain cluster can no longer be electrochemically active for (1). Note that the GB electrochemical complexions on average evolve in the direction of local electronic conductivity \downarrow (SOHe \downarrow) with cycling. If the liquid electrolyte has dried out, there will also be Li/Li^+ conductivity $\downarrow\downarrow$, and SOHi drops to zero. Such SOHi failure could be reversed once new liquid electrolyte is injected to provide percolating Li^+ (electrolyte) transport. In contrast, SOHe drops to zero when the metal fragments into pieces, cutting off supply of e^- (metallic), and SOHe failure would not be easily repairable as it involves the damage of solid components. Therefore, experimentally, SOHe should be tracked carefully *in situ* (by for instance in-plane electronic measurements, see below), in particular for binder-free and conductive-agent free foil electrodes, where GBs play the dual role of binders and conductive agents to active regions in (1).

We expect porosity (p) evolution of the foil to be a key factor controlling SOHe, which can be independently estimated (see below), in particular right after the chemo-mechanical shock:



from mechanical prelithiation. We will show that such chemomechanical shock induces ultrananocrystallization of the $\text{LiAl}_{\text{Cubic}}$ product phase on the right-hand side, which will have profound effect on subsequent electrochemical cycling

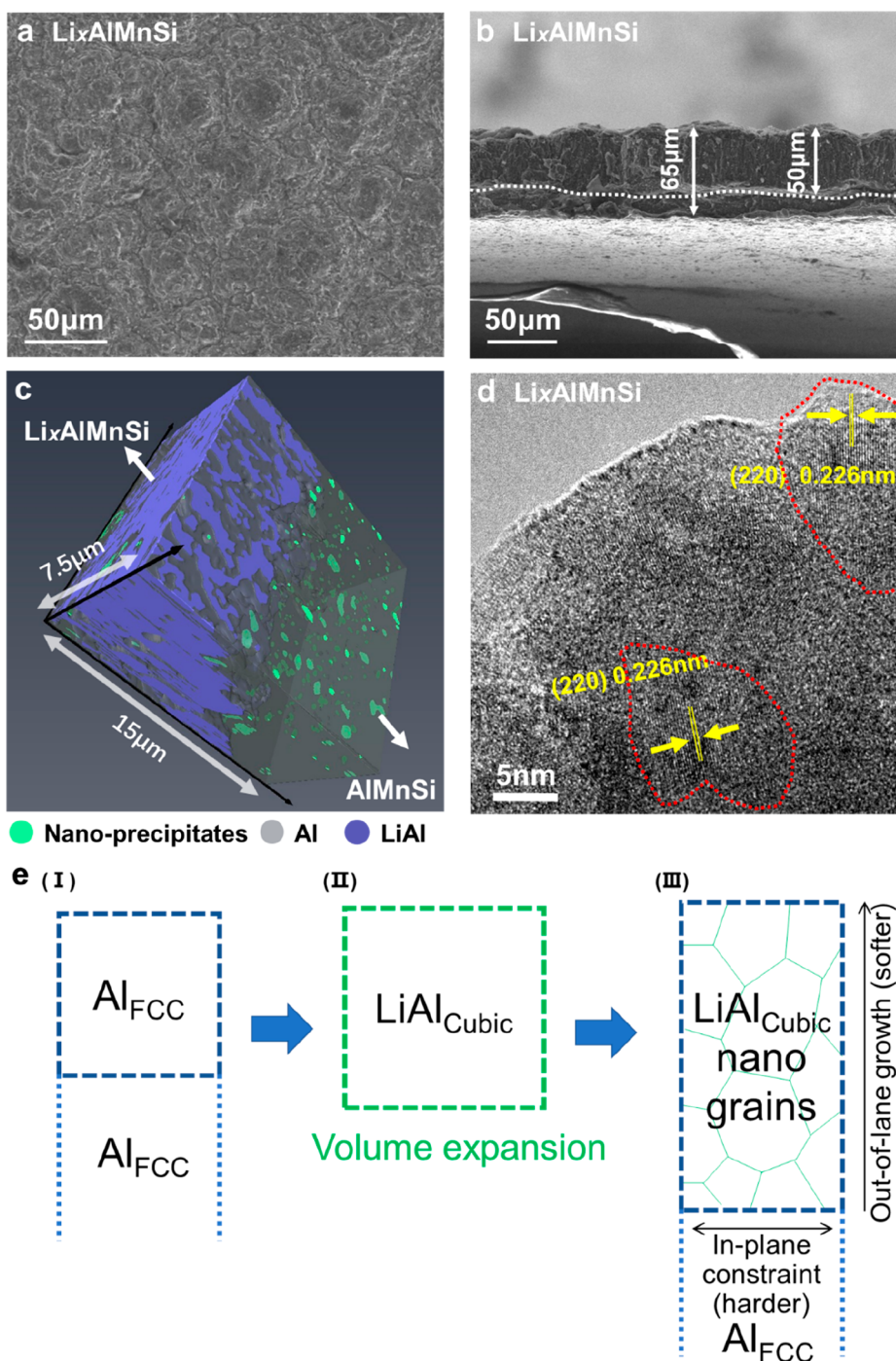


Figure 2. Characterization of Li_xAlMnSi foil. (a) Top SEM view of Li_xAlMnSi foil. (b) Cross-sectional SEM view of Li_xAlMnSi foil. (c) FIB-SEM serial-sectioning 3D reconstruction of Li_xAlMnSi foil. (d) TEM characterization of the Li_xAlMnSi foil. (e) Illustration of the formation of ultrananocrystallization of LiAl phase during the MP.

kinetics, based on the GB electrochemical complexion discussions above. Porosity, which characterizes damage and SOHe, will be shown to be significantly improved by minor addition of dopants (1–2 wt % Mn, Si) before MP that refines the initial Al_{FCC} grain size and provides more GB network for Li diffusion and stress relaxation to accommodate the chemomechanical shock and nanocrystallization. These intriguing relationships provide valuable insights for designing long-lived foil anodes.

In subsequent electrochemical cycling, all three factors ($\text{SOHe} \times \text{SOHi} \times \text{LiInv}$) of the foil anode are indispensable.

They are indeed the critical concerns of any full-cell electrode, whether it is powder slurry, alloy foil, or pure Li_{BCC} foil. Particularly, in foil systems, the evolution of GB electrochemical complexion needs to reach a fine balance between increasing SOHi and decreasing SOHe to make full use of LiInv. We find that coarse-grained pure Al foil after MP is incapable to achieve this kind of gentle balance, as we applied a facile roll-to-roll MP process (Figure S1a). Li_xAl foil (characterized by XRD in Figure S1b) is fragile and tends to disintegrate into fragments (Figure S1c) right after MP, with larger porosity and damaged electronic percolation from the

outset. SEM inspection (Figure S1d,e) reveals widely distributed, deep cracks, which would lead to poor electrolyte localization (EL)⁵ and lithiation/delithiation ductility (LDD) properties. We believe the unacceptably large porosity (close to 30%, as shown next) of MPed Li_xAl foil results from insufficient GB sliding systems that failed to relieve the phase transformation stress generated during chemomechanical shock (2). Electron backscattered diffraction (EBSD) imaging of the pure Al foil before MP is shown in Figure S1f, where only several ~50 μm sized grains and GB network could be observed. Note that such coarse grain size is comparable to the foil thickness (40 μm) itself; thus, phase transformation could easily propagate along one coarse GB all the way to the bottom to penetrate the foil during MP, bringing about greater risk of cutting off e⁻ (metallic) transfer in one swoop. Thus, this result compels us to explore a better chemomechanical shock accommodation strategy (better “shock absorber”) to maintain good LDD and a healthy SOHe in foil systems.

In this work, commercially available AlMnSi alloy, which is doped with 1–2 wt % Mn and Si, was chosen as the starting material. We expect that these doping elements precipitate out in the form of second-phase nanoparticles, which have a well-known Zener pinning and grain refinement effect in polycrystalline materials by pinning down the motion of GBs.^{20,21} Transmission electron microscopy (TEM) was adopted to characterize its microstructure. As shown in Figure 1a, some precipitates with a size of ~100 nm (marked with yellow arrows) are located at the GBs in AlMnSi foil. In pure Al foil, in contrast, only a few dislocations were found in Figure S2. The nanoprecipitates were identified as α-(AlMnSi) and Al₆Mn by X-ray diffraction (XRD) in Figure S3, matching well with the equilibrium phase diagram.^{22,23} Furthermore, 3D serial-sectioning FIB-SEM was employed to show the population of nanoparticles in the foil. From the 3D reconstruction and 2D backscatter electron mode (BSE) images (Figure 1b,c), we could find many nanoprecipitates distributed in the foil, consistent with the TEM observations. The grain size of AlMnSi is reduced to ~10 μm, as revealed in EBSD (Figure 1d). We anticipate the denser GB network would enhance shock absorbing capability in MP, as we will show in the following.

AlMnSi foil with the same thickness as pure Al foil (40 μm) was mechanically prelithiated by a high-pressure rolling machine at 30 MPa (as illustrated in Figure S1a), where two pieces of the starting foil sandwiched a 50 μm thick Li_{BCC} foil in the middle. Because of mechanical pressure and resulting reaction heat, MP readily proceeded, consuming the Li_{BCC} foil completely. The lithiation products were characterized by XRD (Figure S4a), confirming the existence of LiAl_{Cubic} phase (JCPDS No. 65–3017). The laminate could be easily separated into two pieces of free-standing Li_xAlMnSi foils with mechanical peeling, and one of them is shown in Figure S4c. Surprisingly, unlike the rough and fragile Li_xAl foil (Figure S1c,d, surface roughness is 2.0 μm, Table S1), the as-obtained Li_xAlMnSi foil shows smoother surface (Figure S4d, surface roughness is 1.4 μm, Table S2) and an optically intact structure by visual inspection (Figure S4d). SEM observation in Figures 2a and S4c display no apparent cracks (at the SEM resolution, which is few nanometers), indicating the increased GB sliding system was able to accommodate the chemomechanical shock and release phase transformation stress generated during MP quite well.

Compared to the severely damaged Li_xAl foil (Figure S1d), SEM of the nanocrystalline Li_xAlMnSi foil is shown in Figure S5. Some nanoscale pores can be seen on the surface, but they are clearly different from the deep and long cracks in pure Li_xAl (Figure S1d). Most of the ultrananocrystalline LiAl/LiAl GBs in Li_xAlMnSi are not cracked, providing no electrolyte ingress access, but aid Li transport by the extra free volume inside. We then quantitatively measure the porosity or total “free-volume” that is caused by the chemomechanical shock of AlMnSi and pure Al during MP. First, presuming no porosity is generated during MP, and no lateral expansion, the theoretical thickness is calculated. From *ab initio* calculations (materialsproject.org), Li_{BCC} (mp-135) has volume per Li atom of 20.121 Å³, Al_{FCC} (mp-134) has volume per Al atom of 16.472 Å³, and LiAl_{Cubic} (mp-1067) has volume per LiAl of 32.103 Å³, almost double that of Al_{FCC} and which is the basis for the shock. Therefore, to absorb 25 μm worth of Li_{BCC} at least (16.472/20.121) × 25 μm = 20.47 μm worth of Al_{FCC} is needed for the reaction, forming 39.887 μm worth of LiAl_{Cubic} and leaving 40 – 20.47 = 19.53 μm of unreacted Al_{FCC} (as-received AlMnSi/Al foil is 40 μm thick). The ideal thickness of the Li_xAlMnSi and Li_xAl foils is supposed to be 39.887 + 19.53 = 59.4 μm after the reaction if no porosity and no lateral expansion are involved.

Then the actual apparent thicknesses of Li_xAlMnSi and Li_xAl samples are measured and shown in Table S3. The total apparent thickness is decomposed into the apparent reacted layer thickness and the unreacted layer thickness: $t_{\text{total}} = t_{\text{react}} + t_{\text{unrea}}$. Independent measurements are performed at different locations of the foil to not only obtain the average $E[t]$ but also the standard deviation $\sigma[t]$ (the value behind the \pm in Table S4). Note that when measuring t_{react} and t_{unrea} , 20 random spots were selected (Figure S6). Additionally, however, we notice there actually can be some lateral areal expansion (Table S5) during MP, meaning there can be sample-wide plastic deformation in both in-plane x, y and out-of-plane z . We therefore define

$$\alpha \equiv \text{area}(\text{after MP}) / \text{area}(\text{before MP}) \quad (3)$$

and find $\alpha = 1.228$ for pure Li_xAl, but it is very close to 1.0 in Li_xAlMnSi (Table S5). We can then calculate the porosity within the apparent reacted layer

$$p \equiv (E[t_{\text{total}}] - 59.4 \mu\text{m}/\alpha) / E[t_{\text{react}}] \quad (4)$$

as the unreacted layer is clearly still fully dense and find that $p_{\text{LiAl}} = 18.1 \mu\text{m} / 66.5 \mu\text{m} = 27.2\%$, which is a huge amount of porosity, approaching that of slurry coatings (even though we profess to make a foil anode, in Figure S1). In contrast, $p_{\text{LiAlMnSi}} = 5.6 \mu\text{m} / 50.6 \mu\text{m} = 11.0\%$, which is much less damaging, considering not all free volume belong to open pores, and much of the 11.0% could be trapped inside the ultrananocrystalline LiAl/LiAl GBs that facilitate Li GB diffusion but do not allow liquid electrolyte invasion.

Cross-sectional SEM in Figure 2b shows that in Li_xAlMnSi, the total thickness increases to $E[t_{\text{total}}] = 65.0 \mu\text{m}$ after MP, with a $E[t_{\text{react}}] = 50.6 \mu\text{m}$ apparent reacted layer, and $E[t_{\text{unrea}}] = 14.4 \mu\text{m}$ AlMnSi layer. Note that MP could be controlled by tuning the mechanical pressure, and the electrochemically retrievable LiInv generally increases as mechanical pressure increases, as demonstrated in Table S6. When adopting 30 MPa pressure here, the MP degree (characterized by x value in Li_xAlMnSi) is estimated to reach the saturation limit of 0.751 by molar ratio (calculation details could be found in Table S7).

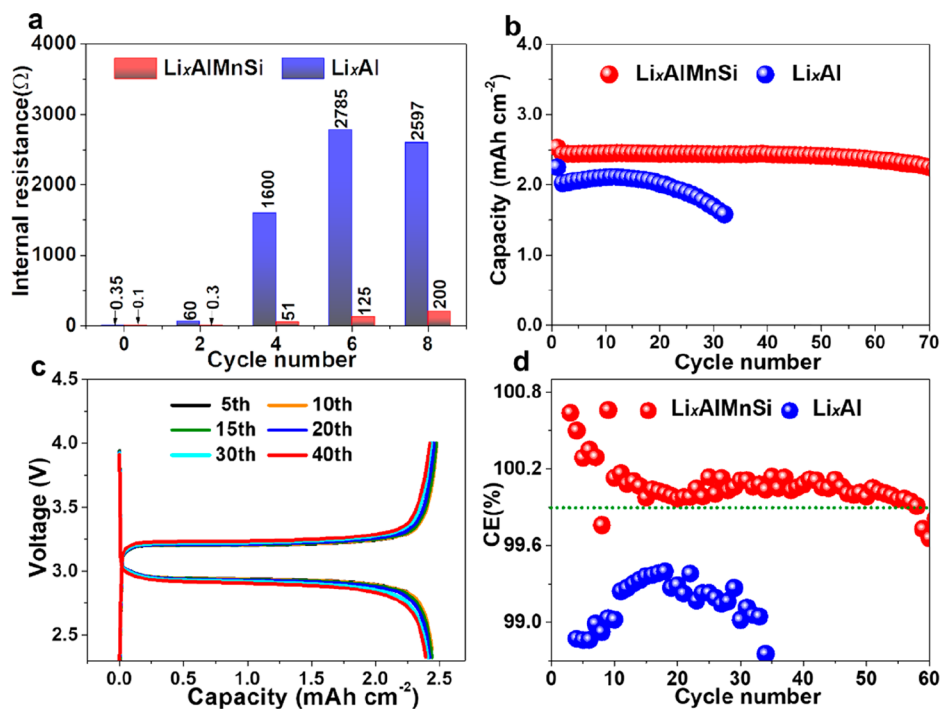


Figure 3. SOHe and electrochemical performance of the $\text{Li}_x\text{AlMnSi}/\text{Li}_x\text{Al}$ foils. (a) Histogram chart of SOHe of Li_xAl and Li_xAlMnSi foil. (b) Cycling performance comparison between $\text{LFP}||\text{Li}_x\text{Al}$ and $\text{LFP}||\text{Li}_x\text{AlMnSi}$ full cells. (c) Voltage profiles of $\text{LFP}||\text{Li}_x\text{AlMnSi}$ full cells. (d) Coulombic efficiency comparison of $\text{LFP}||\text{Li}_x\text{Al}$ and $\text{LFP}||\text{Li}_x\text{AlMnSi}$ full cells.

We find there are also $19.53/\alpha - 14.4 = 5.13 \mu\text{m}$ of unreacted Al_{FCC} retained within t_{react} which accounts for $5.13/50.6 = 10\%$ volume. Just like the retained austenite phase after martensitic transformation of steels can improve the ductility of steel, we believe the retained Al_{FCC} phase in t_{react} improves its LDD. It means the measured $E[t_{\text{react}}] = 50.6 \mu\text{m}$ layer consists of 11 vol % porosity, 10 vol % retained Al_{FCC} , and 79 vol % LiAl , while the intact $E[t_{\text{unrea}}] = 14.4 \mu\text{m}$ layer is 100% Al_{FCC} , consistent with the FIB-SEM serial-sectioning observation in Figure S4b and 3D reconstruction image in Figure 2c. The pure Li_xAl case also has retained Al_{FCC} inside, but that is to no avail in terms of ductility because the 27.2% porosity after shock in the form of long, deep cracks (Figure S1) would negate any beneficial effect of retained ductile FCC phase. The above proves our claim that the initial shock damage of metal foils during MP is much reduced, with the introduction of minute amount of nanoparticles that enables the refined grain size from $\sim 50 \mu\text{m}$ of pure Al to $\sim 10 \mu\text{m}$ of AlMnSi . On the basis of this, one could confidently foresee better LDD/SOHe behavior in Li_xAlMnSi foil than in Li_xAl foil during subsequent electrochemical cycling.

Interestingly, after carefully examining our LiAl phase with XRD (Figure S4a) and TEM (Figure 2d), we find the lithiation product is ultrananocrystalline right after MP. On the basis of Scherrer equation: $L = K \lambda / (\text{FWHM} \times \cos \theta)$, where the calculation parameters are listed in Table S8, we could obtain that average crystal size of LiAl in Li_xAlMnSi foil is $\sim 25 \text{ nm}$. Such nanograin characteristics of LiAl after chemomechanical shock (2) seem to be at the heart of the phase transformation during MP. It should profoundly affect subsequent electrochemical cycling by changing the effective Li diffusivity through the ample LiAl/LiAl GBs, as discussed previously. The formation of the nanograin LiAl in MP is the result of chemomechanical shock,¹³ akin to nanocrystallization of

metals in well-known severe plastic deformation (SPD) processing like equal channel angular extrusion (ECAP).²⁴ In both cases, there is injection and dissipation of large amount of mechanical energy, there is severe geometry constraint, and the transformation occurs near room temperature. The main difference is that here, in MP, the volume change and stress are generated by chemomechanical shock brought by metallurgical reaction 2. We know from EBSD that AlMnSi had $10 \mu\text{m}$ -scale grains right before MP (Figure 1d) that are already refined by the Mn or Si nanoprecipitates compared to the $50 \mu\text{m}$ -scale grains of pure Al (Figure S1f) but still quite large. To understand how 25 nm scale “nano” LiAl was generated in a cubic-to-cubic phase transformation (2), we need to appreciate the constraints in this system (as illustrated in Figure 2e). The phase transformation propagates as a front from the Li_{BCC} side to the interior. The LiAl (cubic) entails a $\sim 100\%$ volume expansion (Figure 2e I and II), but it cannot expand isotropically, as it is constrained on the bottom (Figure 2e I and III). It needs to expand mostly uniaxially upward, as the Li_{BCC} phase on top has a much softer yield strength (few MPa) than the Al_{FCC} phase (few hundred MPa) on the bottom. To do this, it needs to break up into orientational domains (e.g., grains) to fit into the designated box. It is akin to breaking up a big sugar cube to pour the sugar fragments into a tall glass (whose footprint is compatible with the bottom, harder constraint). The fact that the measured $\alpha_{\text{LiAl}} = 1.228$ but $\alpha_{\text{LiAlMnSi}} = 1.0$ means that the 1–2 wt % Mn and Si dopants significantly harden the not-yet-transformed substrate in Figure 2e as it is under in-plane tension during MP, preventing its stretching and damage.

Unlike slurry-casting electrodes, which usually have at least 30% porosity that facilitates electrolyte percolation and SOHi, it is critical for the lithiated foil to have sufficient lithium transport paths so as to afford long-range Li supply (SOHi) for

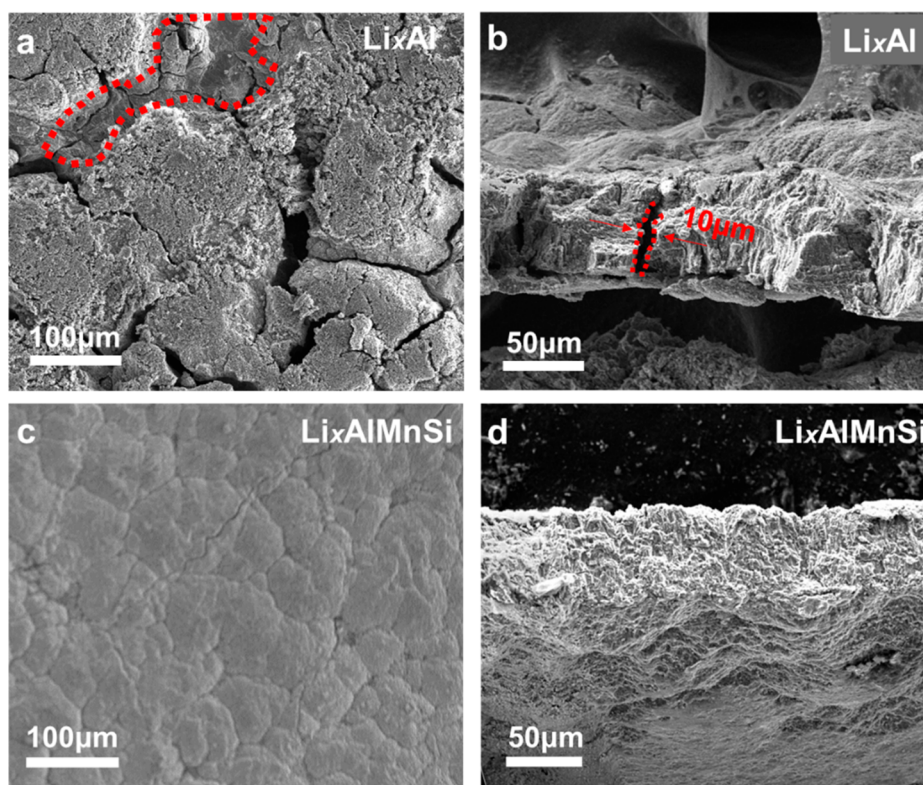


Figure 4. Post-mortem examination of metal foil anodes after 20 cycles. (a) Top surface SEM image of the Li_xAl foil. (b) Cross-sectional image of the Li_xAl foil. (c) Top surface image of the Li_xAlMnSi foil. (d) Cross-sectional image of the Li_xAlMnSi foil.

sustainable electrochemical cycling. Post-mortem examination is carried out on the Li_xAlMnSi anode that was electrochemically lithiated/delithiated just once. After disassembling the cell and directly drying out the electrolyte solvent on/in the anode without further washing so as to “freeze” the electrolyte salt, EDS inspection was conducted to investigate the distribution of fluorine element, the characteristic element of the electrolyte, along the depth direction. The cross-sectional SEM image of the electrode after the first cycle is shown in Figure S7a, which reveals a relatively dense feature without long and deep cracks. Combined with the EDS mapping in Figure S7b, two consecutive layers, including upper Li_xAlMnSi ($\sim 52 \mu\text{m}$) layer and bottom unreacted AlMnSi ($\sim 16 \mu\text{m}$) layer, are evidently identified, suggesting that electrolyte does percolated deep into the 11% porosity of the reacted Li_xAlMnSi layer. Therefore, long-range Li^+ transportation and the global SOHi are ensured in the ultrananocrystalline, long-crack free Li_xAlMnSi foil. Besides, we also measured electrolyte wettability of Li_xAlMnSi foil, which seems to be much improved right after MP, as reflected by the significantly decreased contact angle (Figure S7c,d). Such better electrolyte wettability would also facilitate uniform distribution of electrolyte and reduce the propensity for electrolyte localization (EL),⁵ which is highly damaging to the foil both in terms of SOHi and SOHe.

Generally speaking, liquid electrolyte percolation in the anode is bound to affect SOHe, since the liquid electrolyte or SEI is electronically insulating, as it penetrates into the pores including short or long GB gaps and cracks and forms insulating SEI layers, hindering e^- (metallic) to hop across. It might not be a problem for fine grains or very thin SEI because insulation of one of them has little impact on the global e^-

conductivity when the rest of grains still maintain electronic contact and because electrons may tunnel through thin SEIs of 1–3 nm thickness. However, wider fissures (width on the order of tens of nm) would be impossible for electron to tunnel through. Therefore, we quantitatively monitor the evolution of electron conduction (SOHe) of Li_xAl and Li_xAlMnSi foils during cycling with a three-electrode pouch cell prototype (experimental details in Figure S8). The in-plane SOHe test results at different cycles are shown in Figure 3a, where both Li_xAl and Li_xAlMnSi anodes are starting with initially small resistance $< 1 \Omega$. However, the resistance of Li_xAl foil increases dramatically with electrochemical cycling and reaches up to 2785 Ω after only 6 cycles, which indicates that the in-plane electron hopping is starting to encounter great resistance. In contrast, Li_xAlMnSi anode shows only slight increase and remains at between 100 and 200 Ω in the first 20 cycles (Figure S8), revealing stability in SOHe of Li_xAlMnSi even if nanocracks may be generated (as we will show later) to imbibe liquid electrolyte, forming patches of SEI, which, however, seem to be thin (and narrow) enough that electron can tunnel through GBs.

From the investigation above, with the same LiInv (Figure S9a), enhanced electrochemical cycling stability is expected for Li_xAlMnSi . To verify this, we have assembled $\text{LiFePO}_4 \parallel \text{Li}_x\text{AlMnSi}$ and $\text{LiFePO}_4 \parallel \text{Li}_x\text{Al}$ full cells. The initial charge/discharge curves of the two kinds of cells are shown in Figure S10a, from which we discovered that they showed almost the same charge capacities but different discharge capacities, where the $\text{LFP} \parallel \text{Li}_x\text{Al}$ shows 2.2 mAh cm^{-2} first-cycle discharge capacity (ICE = 77.8%), and the $\text{LFP} \parallel \text{Li}_x\text{AlMnSi}$ full cell shows 2.35 mAh cm^{-2} first-cycle discharge capacity (ICE = 87.7%). Such discrepancy in first-cycle capacity can be induced

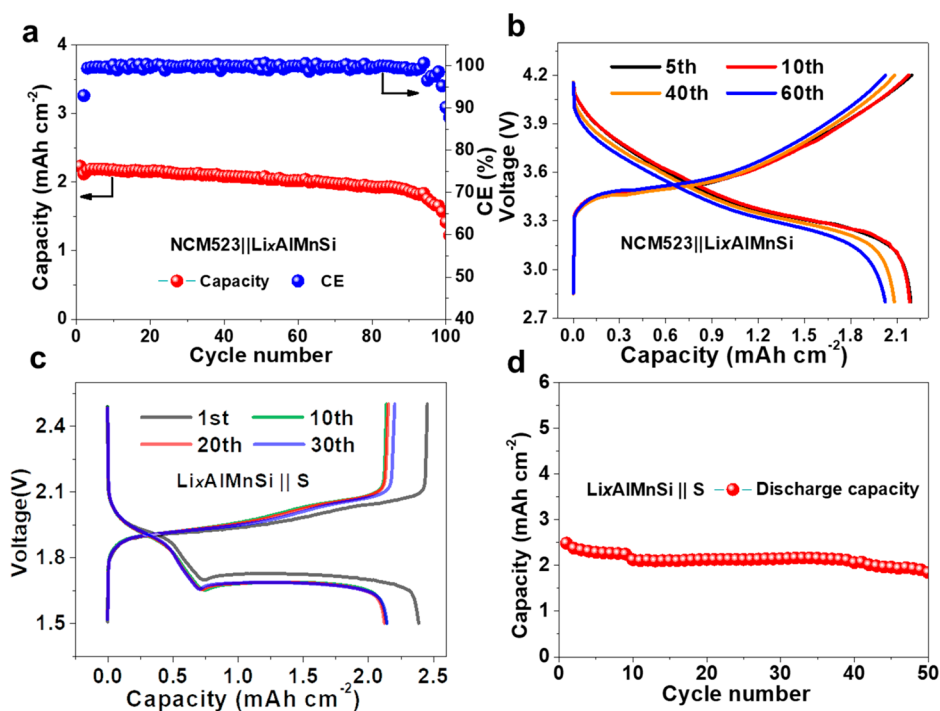


Figure 5. Electrochemical performance of the ultrananocrystalline Li_xAlMnSi anodes. (a) Cycling performance in high voltage Ni-rich full cells. (b) Voltage profiles of NCM523 || Li_xAlMnSi full cells. (c) $\text{Li}_x\text{AlMnSi}||\text{S}$ voltage profiles. (d) $\text{Li}_x\text{AlMnSi}||\text{S}$ full cells cycling performance.

by parasitic reactions with electrolyte, or by some kind of impedance, or both,^{25,26} and Figure S10 discussed this discrepancy in detail from the perspective of cracking.

In long cycling, which is most critical for rechargeable batteries, the LFP|| Li_xAlMnSi full-cell can maintain 90% retention after 70 cycles (Figure 3b). In contrast, the Li_xAl anode starts to decay from the 10th cycle and reaches 80% capacity even before the 30th cycle. The voltage profiles of LFP|| Li_xAlMnSi full cells in Figure 3c exhibit stable working voltage platform between 2.3 and 4.0 V, while the Li_xAl shows a severe polarization, resulting in an evident reduction of discharge voltage platform to around 2.7 V at around the 30th cycle (Figure S9b). The same trend is also reflected in the CE as shown in Figure 3d, where Li_xAlMnSi comes with an extremely high CE, exceeding 99.9% for more than 60 cycles, but CE of the Li_xAl is always lower than 99.5% and plunges dramatically at around 20 cycles. Such a big difference in CE performance was discussed in detail with the aid of EIS measurements in Figure S11. Notably, the Li_xAlMnSi -based lithiated foil enhanced the cycle life of full cells by three time compared to Li_xAl anode and was well adapted to various current densities (Figure S12).

Such dramatic improvements in electrochemical performance compel us to look further into microstructural disparities after electrochemical cycling. Although large volume change happens locally for the Li_xAlMnSi anode due to the nature of the alloying reaction 1, we find that the apparent volume expansion seems to be mitigated, as amply revealed in Figure S13. Then post-mortem examination is carried out on metal foils upon further cycling. We found that the Li_xAl anode has been torn apart into small pieces after just 10 cycles, and the broken structure contrasts sharply with the intact Li_xAlMnSi anode (Figure S14). After 20 cycles, an isolated piece of the broken Li_xAl anode was examined by SEM, which presented a rugged cracked surface with electrolyte localization⁵ phenom-

enon (unreacted area marked with red dot line in Figure 4a), where the marked area is deprived of liquid electrolyte and does not contribute capacity. As the electrolyte localizes, it concentrates drastic phase transformation there, deteriorating the structural integrity even further of the already mechanically poor Li_xAl foil (Figure S1c). Thus, the cross-sectional image of Li_xAl after 20 cycles (Figure 4b) reveals a 10 μm wide crack that cuts through the whole foil. Once coarse grains were fully packed with insulating liquid electrolyte or thick SEI layers, electron tunneling and interfacial Li^+ transportation are no longer feasible, degrading the local SOHe and global SOHi. Eventually, this grain cluster becomes electrochemically inactive, which is reflected by the increase in interfacial resistance (Figure S15a) and well consistent with the as-mentioned SOHe measurement in Figure 3a. In striking contrast, after 20 deep charge/discharge cycles, Li_xAlMnSi anode still exhibits compact structure without conspicuous cracks or electrolyte localization area (Figure 4c,d), demonstrating clearly enhanced LDD. Note that there is also increase in the interfacial resistance with prolonged cycling, but the increment is much gradual than the Li_xAl anode (Figure S15). We speculate that such improvement intrinsically originated from the dense GB network in the ultrananocrystalline Li_xAlMnSi that provides sufficient sliding system for stress relief to ensure a relatively mechanically intact structure with more stable SEI and less void/gas pores that prevent the rendezvous of e^- (metallic) and Li^+ (electrolyte). Here, instead of sustaining a single chemomechanical shock (2) in a matter of tens of seconds in MP, the foil sustains up to hundreds of electrochemomechanical shocks brought by (1), each thousands of seconds in duration, and the Li_xAlMnSi anode, with its myriad of ultrananocrystalline GBs and phase boundaries (PB), behaves quite admirably.

To demonstrate potentially wide applications of Li_xAlMnSi foil anode, we paired it against the higher-voltage 4 V class

cathodes such as Ni-rich nickel cobalt manganese oxide (NCM523) cathodes with an areal capacity of 2.4 mAh cm⁻². In NCM523||Li_xAlMnSi full cells, it keeps 80% initial capacity after 90 cycles (Figure 5a). Voltage profiles in Figure 5b evidenced its high voltage stability when charging the full cell to 4.2 V. Furthermore, the Li_xAlMnSi||NMC523 full cell exhibited good rate performance when cycling at various currents from 0.8 to 12 mA cm⁻², as shown in Figure S16a, in which the discharge capacity is 2.3 mAh cm⁻² at 0.8 mA cm⁻² (0.3C). Even at high current density of 12 mA cm⁻² (5C), the discharge capacity still maintains 1.0 mAh cm⁻². Moreover, when the current density decreased, its capacity recovered to initial level immediately and rose back to 2.25 mAh cm⁻² at the current density of 0.3C (0.8 mA cm⁻²).

Also, it is worth mentioning that the Li_xAlMnSi anode is applicable to the ether-based electrolytes too, for example, it can work properly in 1 M LiTFSI in a solution of 1,3-dioxolane (DOL) and 1,2-dimethoxyethane (DME) (volume ratio = 1:1) with 2 wt % LiNO₃ as additive in Li-sulfur batteries. From Figure 5c, it can be seen that the Li_xAlMnSi || S₈ cell works normally, despite the fact that the voltage plateau is ~0.25 V lower than classic Li-S batteries, which is caused by the slightly higher lithiation voltage of Li_xAlMnSi (~0.25 V vs Li⁺/Li, Figure S9a). Such a slightly elevated anode potential would inhibit Li_{BCC} dendrites from precipitating out even at high charging rates, improving battery safety. After 50 cycles, the discharge capacity still stabilizes at an acceptable value of 2.0 mAh cm⁻², corresponding to 80% capacity retention (Figure 5d). Similarly, the rate performance of Li_xAlMnSi||S₈ batteries also is satisfactory (Figure S16b), when the current density increased stepwise from 0.24 to 2.4 mA cm⁻².

Finally, we have fabricated a 3 cm × 3.4 cm pouch cell, where free-standing Li_xAlMnSi anode with two-side utilization is paired against LiCoO₂ cathodes (LCO, areal capacity ~4.0 mAh cm⁻²), to evaluate its energy density. As revealed in Figure S18a, the initial charge and discharge capacity is 86.9 mAh and 72.7 mAh, respectively, corresponding to ICE = 83.65%. Furthermore, we have calculated its gravimetric and volumetric energy density to be 280 Wh kg⁻¹ and 586 Wh L⁻¹, respectively (Table S10), which is quite competitive against commercial lithium ion batteries. Quite stable cycling performance is observed in initial cycles (Figure S18b).

In summary, we propose that lock-step preservation of SOHe, SOHi, and LiInv are essential for long-lived reversible metallic foil anode, and failure in any one of them would terminate reversible electrochemical cycling. By employing a mechanical prelithiation (MP) method to make LiInv >1 initially, the chemomechanical shock from MP creates an ultrananocrystalline LiAl layer. We revealed that a small amount of Mn and Si into Al foil induces nanoprecipitates Zener pinning and the resultant dense GB network before MP greatly reduces the porosity and damage after MP, due to the enhanced transport and reduced stress accumulation during the chemomechanical shock. Afterward, the ultrananocrystalline, long-crack free Li_xAlMnSi foil demonstrates significantly superior electrochemical lithiation/delithiation ductility, improved SOHe, and electrolyte localization, which delay the gross foil fracture and preserve global electronic percolation in the foil. With a robust, multiconnected electron percolation network, ultrananocrystalline Li_xAlMnSi foil anode demonstrates an order-of-magnitude more stable SOHe than Li_xAl foil anode. Full cells against NCM523 and LFP cathodes perform well. It shows great potential for next-generation LIBs

and provides guidelines for developing other metallic foil-based anodes including Li_{BCC} foils.

■ ASSOCIATED CONTENT

Supporting Information

The Supporting Information is available free of charge at <https://pubs.acs.org/doi/10.1021/acs.nanolett.9b03626>.

Experimental details, schematic diagram, XRD patterns, optical photographs, top-view SEM images, cross-sectional image, EBSD image; TEM images, BSE images, SOHe test results, Li inventory, voltage curves, charge/discharge curves, EIS pattern, Coloumbic efficiencies, rate performances, interfacial resistance, batteries performance, thickness measurements, lateral area expansion, prelithiation degree, mole ratio calculation, calculation parameters, parameters of pouch cell (PDF)

■ AUTHOR INFORMATION

Corresponding Authors

*E-mail: lisa@tongji.edu.cn.

*E-mail: liju@mit.edu.

ORCID

Bo Chen: 0000-0001-7515-3042

Ju Li: 0000-0002-7841-8058

Author Contributions

[†]H.F. and B.C. contributed equally to this work.

Notes

The authors declare no competing financial interest.

■ ACKNOWLEDGMENTS

The authors are grateful for the support from Tongji University and the National Natural Science Foundation of China (NSFC-No. 51602222, 51632001 and 51972236). S.L. acknowledges the support by the Fundamental Research Funds for the Central Universities (No. 0500219233); J.L. acknowledges the support by Samsung Advanced Institute of Technology.

■ REFERENCES

- (1) Li, S.; Niu, J.; Zhao, Y. C.; So, K. P.; Wang, C.; Wang, C. A.; Li, J. *Nat. Commun.* **2015**, *6*, 7872.
- (2) Tong, X.; Zhang, F.; Ji, B.; Sheng, M.; Tang, Y. *Adv. Mater.* **2016**, *28*, 9979–9985.
- (3) Wang, M.; Zhang, F.; Lee, C.-S.; Tang, Y. *Adv. Energy Mater.* **2017**, *7*, 1700536.
- (4) Zhang, F.; Ji, B.; Tong, X.; Sheng, M.; Zhang, X.; Lee, C.-S.; Tang, Y. *Adv. Mater. Interfaces* **2016**, *3*, 1600605.
- (5) Jiang, M.; Yu, Y.; Fan, H.; Xu, H.; Zheng, Y.; Huang, Y.; Li, S.; Li, J. *ACS Appl. Mater. Interfaces* **2019**, *11*, 15656–15661.
- (6) Xu, H.; Li, S.; Zhang, C.; Long, C. x.; Jian, L. w.; Yong, X.; Zheng, Y.; Huang, Y.; Li, J. *Energy Environ. Sci.* **2019**, *12*, 2991.
- (7) Sun, J.; Zeng, Q.; Lv, R.; Lv, W.; Yang, Q.-H.; Amal, R.; Wang, D.-W. *Energy Storage Materials.* **2018**, *15*, 209–217.
- (8) Kim, H. J.; Choi, S.; Lee, S. J.; Seo, M. W.; Lee, J. G.; Deniz, E.; Lee, Y. J.; Kim, E. K.; Choi, J. W. *Nano Lett.* **2016**, *16*, 282–8.
- (9) Kim, M.; Xu, F.; Lee, J. H.; Jung, C.; Hong, S. M.; Zhang, Q. M.; Koo, C. M. *J. Mater. Chem. A* **2014**, *2*, 10029–10033.
- (10) Forney, M. W.; Ganter, M. J.; Staub, J. W.; Ridgley, R. D.; Landi, B. J. *Nano Lett.* **2013**, *13*, 4158–63.
- (11) Ai, G.; Wang, Z.; Zhao, H.; Mao, W.; Fu, Y.; Yi, R.; Gao, Y.; Battaglia, V.; Wang, D.; Lopatin, S.; Liu, G. *J. Power Sources* **2016**, *309*, 33–41.

- (12) Cao, Z.; Xu, P.; Zhai, H.; Du, S.; Mandal, J.; Dontigny, M.; Zaghbi, K.; Yang, Y. *Nano Lett.* **2016**, *16*, 7235–7240.
- (13) Zhang, S.; Zhao, K.; Zhu, T.; Li, J. *Prog. Mater. Sci.* **2017**, *89*, 479–521.
- (14) Yang, S.; Yan, B.; Li, T.; Zhu, J.; Lu, L.; Zeng, K. *Phys. Chem. Chem. Phys.* **2015**, *17*, 22235–42.
- (15) Han, S.; Park, J.; Lu, W.; Sastry, A. M. *J. Power Sources* **2013**, *240*, 155–167.
- (16) Zhang, M.; Xiang, L.; Galluzzi, M.; Jiang, C.; Zhang, S.; Li, J.; Tang, Y. *Adv. Mater.* **2019**, *31*, No. e1900826.
- (17) Xu, H.; Li, S.; Chen, X.; Zhang, C.; Liu, W.; Fan, H.; Yu, Y.; Huang, Y.; Li, J. *Adv. Energy Mater.* **2019**, *9*, 1902150.
- (18) Cantwell, P. R.; Tang, M.; Dillon, S. J.; Luo, J.; Rohrer, G. S.; Harmer, M. P. *Acta Mater.* **2014**, *62*, 1–48.
- (19) Xu, G.; Yan, Q.-b.; Kushima, A.; Zhang, X.; Pan, J.; Li, J. *Nano Energy* **2017**, *31*, 568–574.
- (20) Weygand, D.; Bréchet, Y.; Lépinoux, J. *Acta Mater.* **1999**, *47*, 961–970.
- (21) Vetrano, J. S.; Bruemmer, S. M.; Pawlowski, L. M.; Robertson, I. M. *Mater. Sci. Eng., A* **1997**, *238*, 101–107.
- (22) Wei, K. X.; Wei, W.; Du, Q. B.; Hu, J. *Mater. Sci. Eng., A* **2009**, *525*, 55–59.
- (23) Martins, J. P.; Carvalho, A. L. M.; Padilha, A. F. *J. Mater. Sci.* **2009**, *44*, 2966–2976.
- (24) Valiev, R. Z.; Islamgaliev, R. K.; Alexandrov, I. V. *Prog. Mater. Sci.* **2000**, *45*, 103–189.
- (25) Kasnatscheew, J.; Evertz, M.; Streipert, B.; Wagner, R.; Nowak, S.; Cekic Laskovic, I.; Winter, M. *J. Phys. Chem. C* **2017**, *121*, 1521–1529.
- (26) Kasnatscheew, J.; Evertz, M.; Streipert, B.; Wagner, R.; Klopsch, R.; Vortmann, B.; Hahn, H.; Nowak, S.; Amereller, M.; Gentschev, A. C.; Lamp, P.; Winter, M. *Phys. Chem. Chem. Phys.* **2016**, *18*, 3956–65.

■ NOTE ADDED AFTER ASAP PUBLICATION

This paper was posted ASAP on December 20, 2019, without all the authors' corrections applied. The corrected version was reposted on January 13, 2020.

Supporting Information

Nanocrystalline Li-Al-Mn-Si foil as reversible Li host: electronic percolation and electrochemical cycling stability

Huimin Fan^{1,2†}, Bo Chen^{1,3†}, Sa Li^{1,2*}, Yue Yu^{1,2}, Hui Xu^{1,2}, Mengwen Jiang^{1,2}, Yunhui Huang^{1,2}, and Ju Li^{4*}

¹ School of Materials Science and Engineering, Tongji University, Shanghai 201804, China

² Institute of New Energy for Vehicles, Tongji University, Shanghai 201804, China

³ Key Laboratory of Performance Evolution and Control for Engineering Structures of Ministry of Education, Tongji University, 1239 Siping Road, Shanghai 200092, China

⁴ Department of Nuclear Science and Engineering and Department of Materials Science and Engineering, Massachusetts Institute of Technology, Cambridge, MA 02139, USA

†These authors contributed equally to this work

This PDF file includes:

Figures S1 to S18, Tables S1 to S10

Experimental Details

Materials. Pure Al and AlMnSi foils (40 μ m thick); Li_xAl and Li_xAlMnSi were manufactured by mechanical prelithiation, Li (50 μ m) and Al/ AlMnSi (40 μ m) foil were stacked together and got lithiated by rolling machine at different pressure. Commercial one-side coated LiFePO₄ (2.65 mAh cm⁻²), commercial LiNi_{0.5}Co_{0.2}Mn_{0.3}O₂(NCM) (2.4 mAh cm⁻²), with 12mm diameter were used in full cells. Li_xAl electrodes were managed to punched out from the broken structure with great care due to the fragile structure of 65 μ m-thick Li_xAl anode. LiCoO₂ cathodes with 4.0 mAh cm⁻² rated capacity was employed in the pouch cells. 40 μ L of 1M lithium hexafluorophosphate (LiPF₆) in a 1:1 vol/vol mixture of ethylene carbonate (EC) and diethyl carbonate (DEC) with 10 wt.% fluorinated ethylene carbonate (FEC) and 1 wt.% vinylene carbonate (VC) was used as electrolyte. The Li_xAlMnSi/Li//S batteries worked in 40 μ L 1 M LiTFSI in a solution of 1,3-Dioxolane (DOL) and 1,2-Dimethoxyethane (DME) (volume ratio: 1:1) with/without 2 wt% LiNO₃ as additive respectively.

Electrochemical Measurements. Cells were assembled in the CR2025-type coin cells, and the electrochemical performance of cells are carried out by Neware test system (CT-4008, Neware). The Al||Li half-cell was delithiated to 2.3V at a current of 0.3mA cm⁻². The LFP||Li_xAlMnSi/Li_xAl full cells were examined between 2.0V to 4.0V. The electrochemical test on NCM|| Li_xAlMnSi full cells were carried out between 2.5~4.2V. The Li_xAlMnSi/Li//S batteries were test from 1.5 to 2.5V. The electrochemical impedance spectroscopy (EIS) were conducted by Chi660E Electrochemical workstation at a frequency between 0.01–100 KHz (CHI660E, Shanghai Chen Hua Instrument Co., Ltd.).

SOHe test. We quantitatively estimate the ability of electron conduction (SOHe) of the different lithiated foils (Li_xAl/Li_xAlMnSi) at different electrochemical cycling stages. In order to ensure a totally free-standing anode, three electrode-tabs were assembled to test its SOHe with pouch cells instead of coin cells, aiming at eliminating the role of steel housing in current collector. Given the fragile structure of 65 μ m-thick Li_xAl foil, here we fabricated two equal 70 μ m-thick Li_xAl and Li_xAlMnSi foils from initial 50 μ m-thick Al and AlMnSi foil, they can slightly keep an intact structure as the free-standing anodes. The test mode is shown in Figure S8, where two wires were led form the diagonal of anode (Li_xAl/Li_xAlMnSi) to test the in-plane SOHe.

Characterization. The morphologies and structures of Li_xAlMnSi alloy were determined by a field emission scanning electron microscopy (SEM, FEI, QUANTA 250FEG) under an accelerate voltage of 10 kV. XRD measurements were carried out on a Bruker D8-Advance powder X-ray diffractometer operating at 40 kV and 30 mA, using Cu K α radiation ($\lambda = 0.15405$ nm). The signal was collected for diffraction angles (2θ) from 10 $^\circ$ and 80 $^\circ$ at a scan rate of 3 $^\circ$ min⁻¹. The transmission electron microscope (TEM, FEI Talos F200) was performed to determine the grain size on both pristine Al foil and S-Al foil. The electron back-scattered diffraction (EBSD) of

Al/AlMnSi foil were carried out on OXFORD EBSD. The serial-sectioning FIB-SEM were performed by GATAN 3view 2XP instrument. The XPS measurements were carried out on the X-ray photoelectron spectroscopy under Ar-gas protection (XPS, Thermo Scientific Escalab 250Xi).

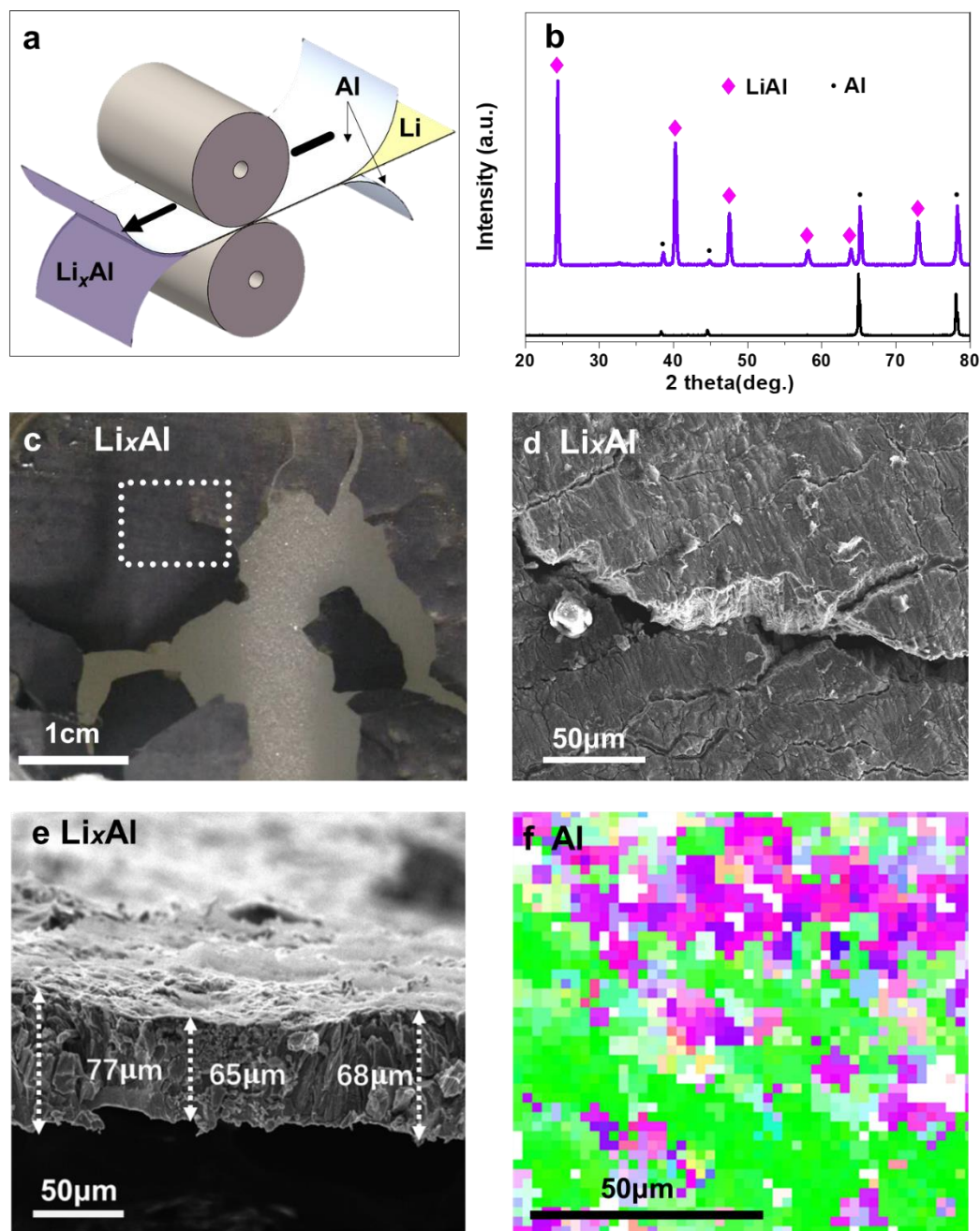


Figure S1. (a) Schematic diagram of roll-to-roll mechanical lithiation process. (b) XRD pattern of the prelithiated pure Al foil. (c) Optical photograph of the as-obtained Li_xAl foil. (d) Top view SEM image of Li_xAl foil. (e) Cross-sectional image of Li_xAl foil. (f) EBSD image of grain size of pure Al foil.

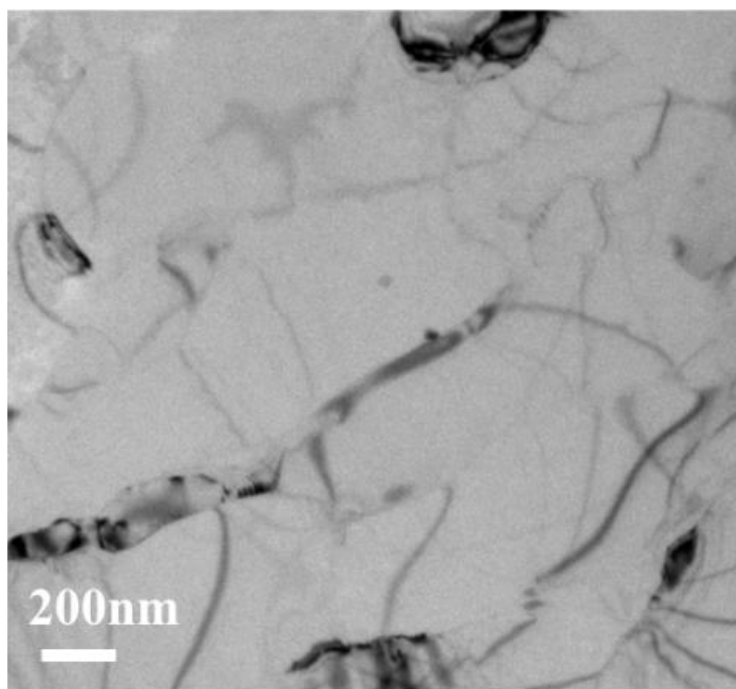


Figure S2. TEM image of pure Al foil.

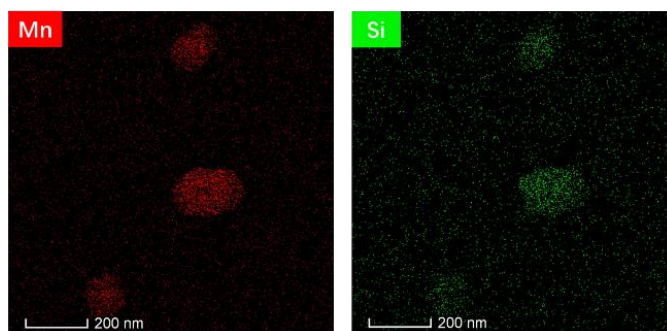
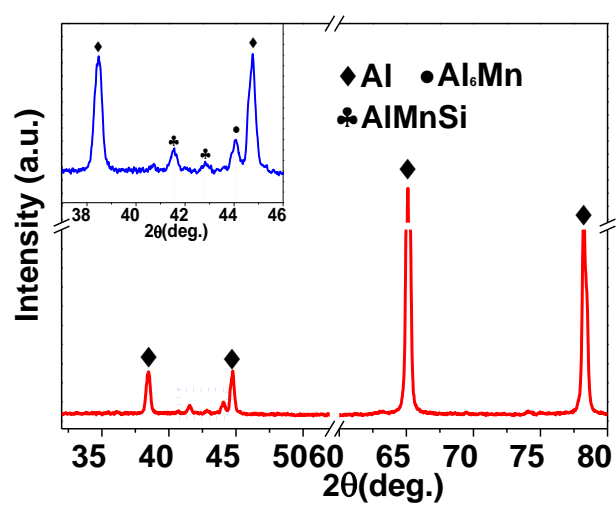


Figure S3. XRD pattern of the AlMnSi foil and EDS mapping of Mn and Si elements.

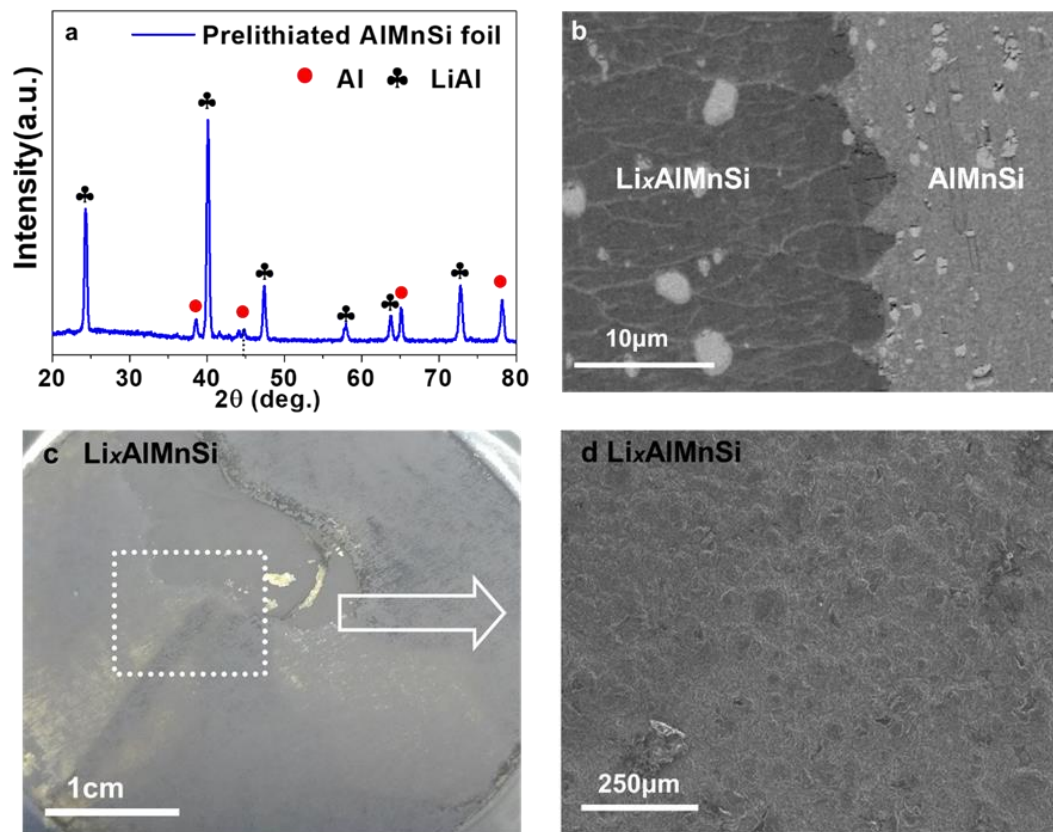


Figure S4. (a) XRD pattern of the prelithiated AlMnSi foil. (b) BSE image of the cross-sectional image of Li_xAlMnSi foil. (c) Optical photograph of the as-obtained Li_xAlMnSi foil. (d) Surface morphology of Li_xAlMnSi foil in large field.

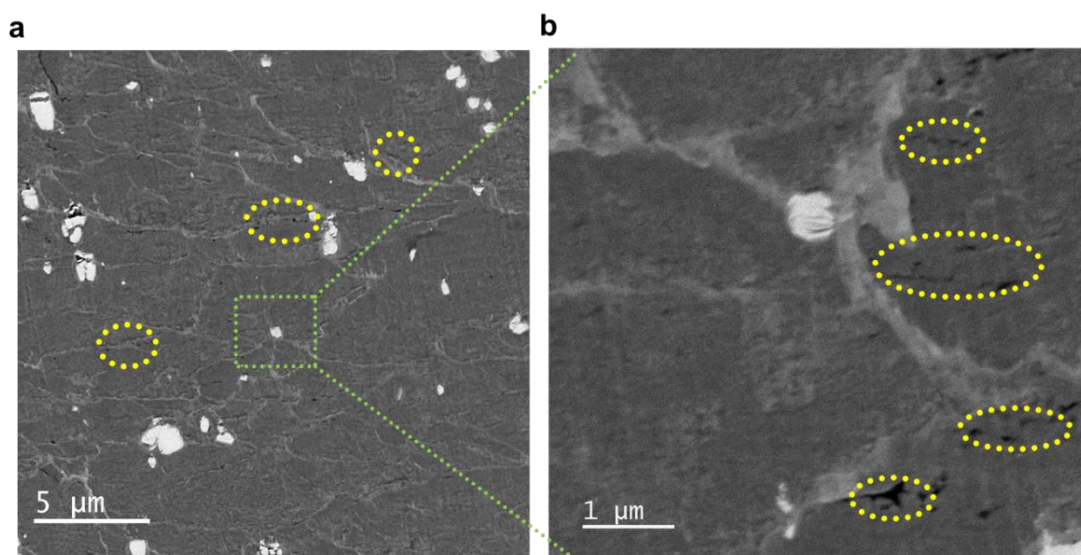


Figure S5. (a) and (b) BSE images of Li_xAlMnSi layer, and the nano scaled “free volume” is marked by yellow circles.

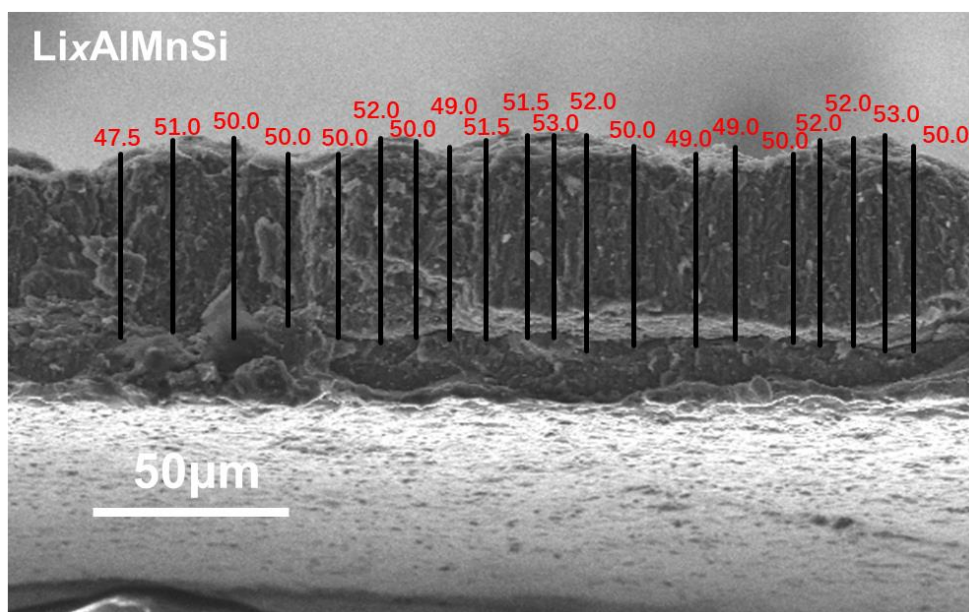


Figure. S6 SEM image of reacted layer thickness measurement of Li_xAlMnSi foil.

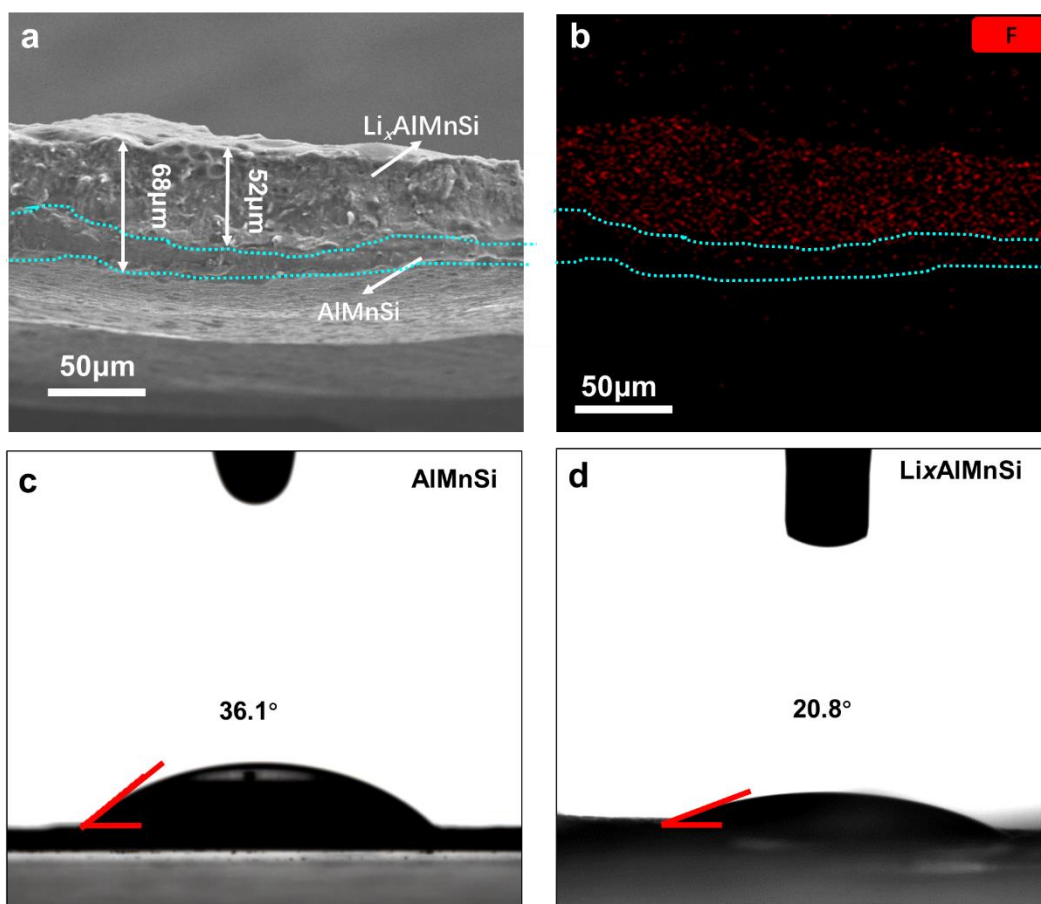


Figure S7. (a) Cross-sectional SEM image of nanocrystalline Li_xAlMnSi after charge/discharge once. (b) Cross-sectional fluorine elements distribution of Li_xAlMnSi after charge/discharge once. Wetting angle of (c) AlMnSi and (d) Li_xAlMnSi foil.

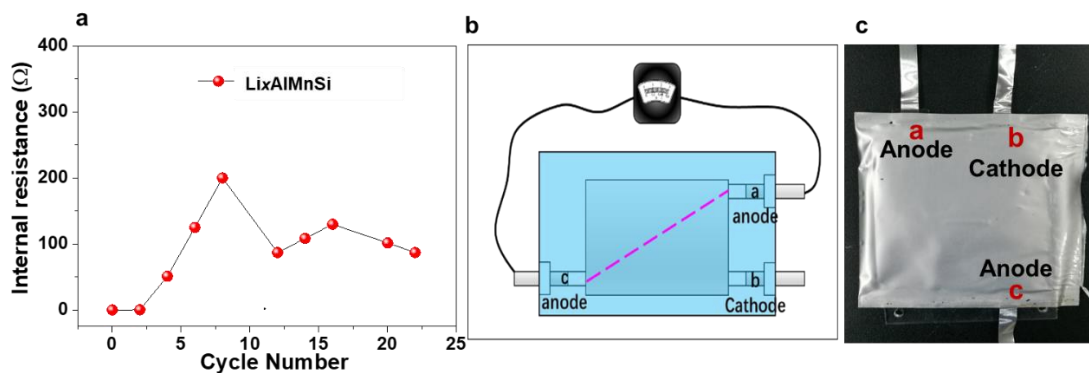


Figure S8. (a) SOHe test results of Li_xAlMnSi anode in the first 20 cycles. (b) and (c) Test mode of the three-electrode pouch cell prototype.

As illustrated in Figure S8 b and c, electrodes a (Li_xAl/Li_xAlMnSi anode) and b (cathode) are used for routine charging/discharging, and after every two cycles, we apply a slight voltage bias across electrode a (Li_xAl/Li_xAlMnSi anode) and c (Li_xAl/Li_xAlMnSi anode), and calculate the resistance across the anode foil by reading the current from the multimeter (Ohm's Law).

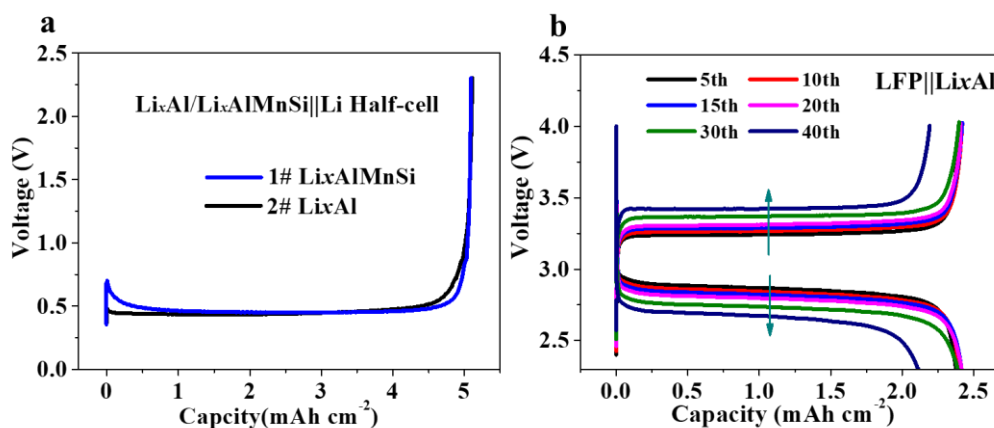


Figure S9. (a) Li inventory of the Li_xAlMnSi and Li_xAl foil. (b) Voltage curves of LFP||Li_xAl full cell during cycling.

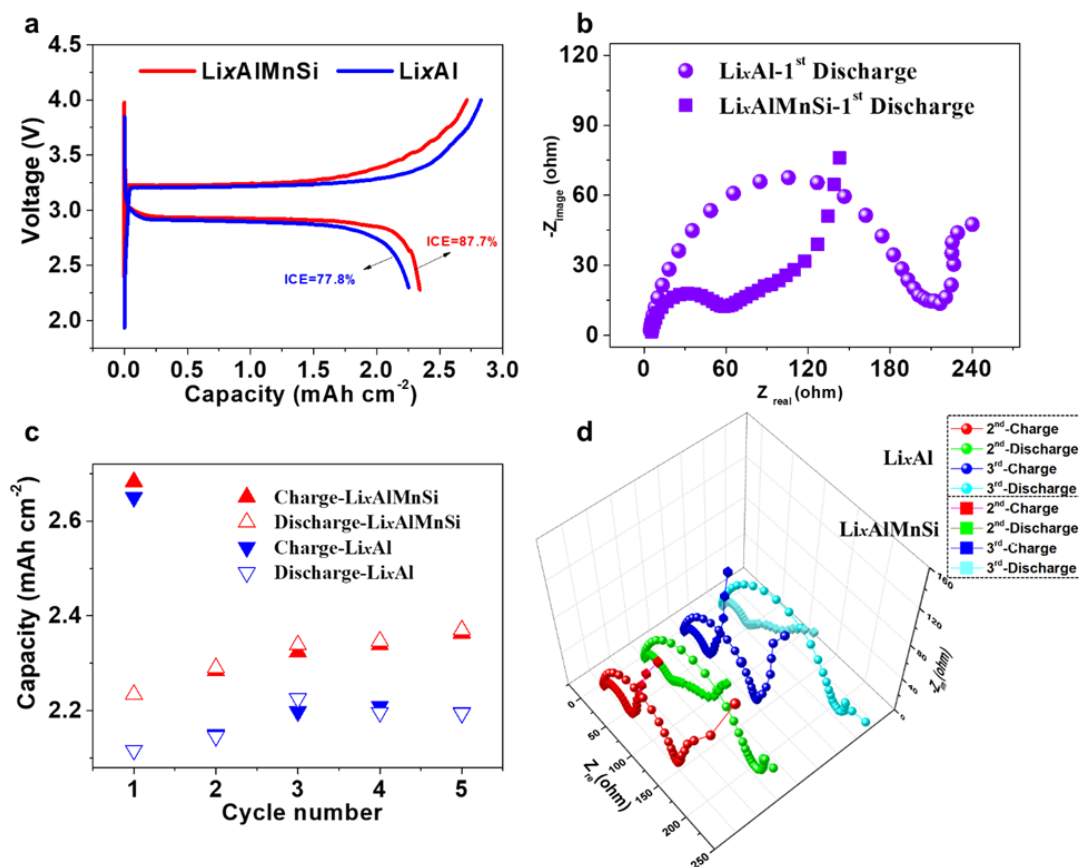


Figure S10. (a) The initial charge/discharge curves of the LFP||Li_xAlMnSi/Li_xAl cells. (b) EIS pattern of LFP||Li_xAlMnSi/Li_xAl full cells at the end of the 1st discharge. (c) Charge/discharge capacity of the LFP||Li_xAlMnSi/Li_xAl cells in the initial cycles. (d) EIS pattern of LFP||Li_xAlMnSi/Li_xAl full cells at the end of charge/discharge state during 2~3 cycles.

We believe such discrepancy in first-cycle capacity can be induced by parasitic reactions with electrolyte, or by some kind of impedance, or both. From the perspective of cracking, more fracture opening is apparently observed in Li_xAl (Figure S1d), which further caused serious parasitic reactions and subsequent capacity degradation during the initial cycle, and therefore bigger capacity loss is expected. One might argue that there is excess active lithium ($1.8 \times$) in the anode at the beginning; however, the problem is whether this LiInv could be “mined” under the condition of fixed cut-off voltage and constant current. To comprehensively understand the underlying kinetic limitations, we examined the impedance through the in-situ EIS test of two kinds of full cells in Figure S10 (b and d). The LFP||Li_xAl full cell exhibits almost four times larger resistance than that of LFP||Li_xAlMnSi cell at the end of first discharge, indicating the bigger delithiation hindrance and subsequently making it more difficult to pump out lithium from Li_xAl anode, even if there is abundant LiInv. Therefore, we could conclude that for the two cells using the same LFP cathodes with excess active lithium ($1.8 \times$), the different capacities during the initial several cycles before LiInv is depleted are mainly originated from the kinetic factors when applying a fixed cut-off voltage and

constant current. Note that the disparate resistance is due to the initial cracked Li_xAl foil (Figure S1c) exposing more free-surface than the intact Li_xAlMnSi foil (Figure 2a) for electrolyte corrosion, significant amount of SEI was formed on the free surface, leading to greater resistance and thus variation in ICE. As a matter of fact, the influence of kinetic factors is also reflected from the capacity and CE of the following several cycles. From Figure S10c, both the charge and discharge capacities of $\text{LFP}||\text{Li}_x\text{AlMnSi}$ cell are superior to that of $\text{LFP}||\text{Li}_x\text{Al}$ cell even though two of them have excess LiInv at that time, which however is well consistent with the impedance results in Figure S10d.

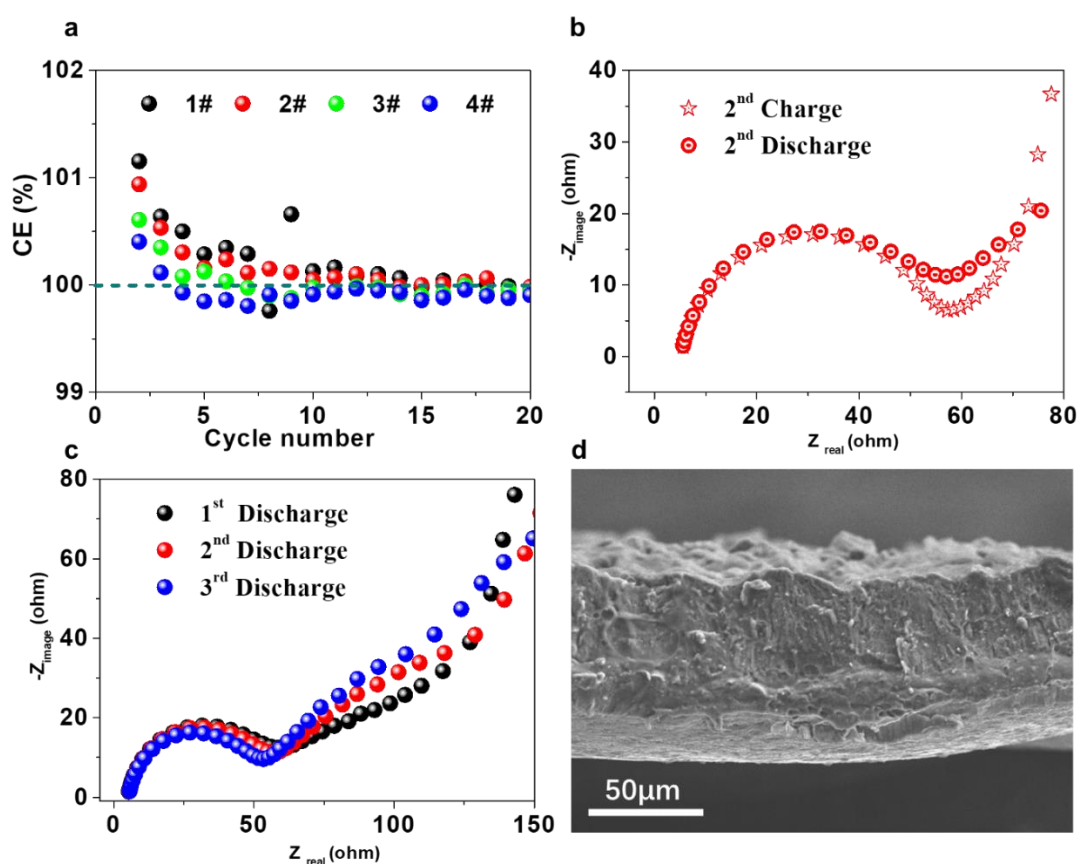


Figure S11. (a) Coulombic efficiency of $\text{LFP}||\text{Li}_x\text{AlMnSi}$ full-cells in the initial cycles. (b) EIS pattern of $\text{LFP}||\text{Li}_x\text{AlMnSi}$ full-cell at the 2nd cycle. (c) EIS pattern of $\text{LFP}||\text{Li}_x\text{AlMnSi}$ full-cell at the end of initial three discharge state. (d) The cross-sectional SEM image of Li_xAlMnSi anode after the initial cycle.

Moreover, we found that the Coulombic efficiencies of all four Li_xAlMnSi samples raised to $>100\%$ in the second cycle, as shown in Figure S11a and Table S9. While this behavior would be uncommon for graphite anode (typically first cycle CE $\sim 90\%$, raising to CE $>99.5\%$ in 5 or so cycles) which does not come with its own LiInv . We think for Li_xAlMnSi anode, which starts with its own LiInv before cycling, this is possible, in a 1st cycle deposit-then-strip / 2nd cycle deposit-then-strip / ... scenario.

Basically, the question is why within fixed full-cell voltage cutoffs [V^{upper} , V^{lower}], one can get more Lithium out of the anode than one can put into that anode, *in a particular cycle*. Note that one will not be violating mass conservation here, because even with the dissipation of cyclable LiInv to non-cyclable Li in SEI, due to the excess inventory (1.8 \times) in Li_xAlMnSi , one can still pump more Li out of the Li_xAlMnSi than one puts in, in the 2nd cycle.

Note that in the 1st cycle before the 2nd cycle, one actually did put more Li into the anode, that one pumped out (CE \sim 87%) – granted, some of those lost are converted into SEI – but it is possible that some of those lost (\sim 13%) are just temporarily unusable because of kinetic limitations¹⁻², in the stripping leg of the 1st cycle. In the depositing part of the 2nd cycle, with the GB sliding that subsequently induces extra free-volume to allow faster Li atom (neutral) GB diffusion, as indicated by the impedance comparison between the cycles in Figure S11b, it is becoming easier and easier to “mine” the Lithium inventory embedded in Li_xAlMnSi . Such kinetic facilitation should help to make the 2nd cycle extraction, 3rd cycle extraction, ... easier, and so in the stripping part of the 2nd cycle, 3rd cycle ..., they can contribute again, to push the CE of the second/third... cycles slightly above 100%. It’s like a business that lost quite a bit of money in the first year, but some of those losses turned out to be exaggerated and are actually investments, that they contribute to a small profit in year 2. Besides, from the low-frequency Warburg resistance shown in Figure S11c, which symbolizes long-range Li diffusion inside the anode’s active material, it is clear that impedance in charge and discharge at the same V are different, for the same cycle, suggesting improved kinetics during discharge, which we speculate is also partly responsible for the additional lithium capacity in the discharging process that makes the discharge/charge ratio (CE) over 100%. The impact of impedance on the apparent capacity and Coulombic efficiency measured at finite rate are elucidated in our previous work^{3,4}.

In addition, for Li_xAlMnSi , based on SEM examination in (Figure S11d), where negligible fracture opening is observed, we reasonably assume that the cracking has not caused serious parasitic reactions and subsequent capacity degradation during initial cycles. Besides, EIS measurement (Figure S11b) that reveals a decrement in delithiation hindrance with prolonged cycles also indicates no severe SEI generation, which otherwise would bring about significant impedance. Considering that the overall capacity fade can be induced either reversibly by kinetic limitations or irreversibly by parasitic reactions due to the cracking, we think both the improved kinetics and insignificant capacity loss from cracking support the CE constantly above 100% in the initial several cycles in Figure S11a.

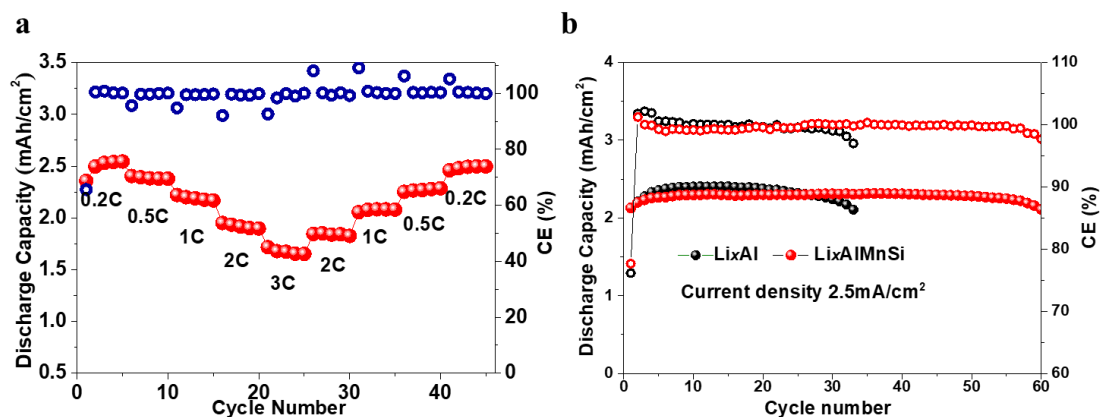


Figure S12. Rate performance of LFP||Li_xAlMnSi full cells (current density ranges from 0.5 mA cm⁻² to 7.5 mA cm⁻²) (a), and at a higher current density of 1C (2.5 mA cm⁻²) (b).

In terms of rate performance, the LFP||Li_xAlMnSi full cells are also well accommodated to current from 0.2C to 3C (current density ranges from 0.5 mA cm⁻² to 7.5 mA cm⁻²) without short circuiting (Figure S12a), and meanwhile, it succeeds in keeping a stable performance for 60 cycles at a higher current density of 2.5 mA cm⁻² (1C) (Figure S12b).

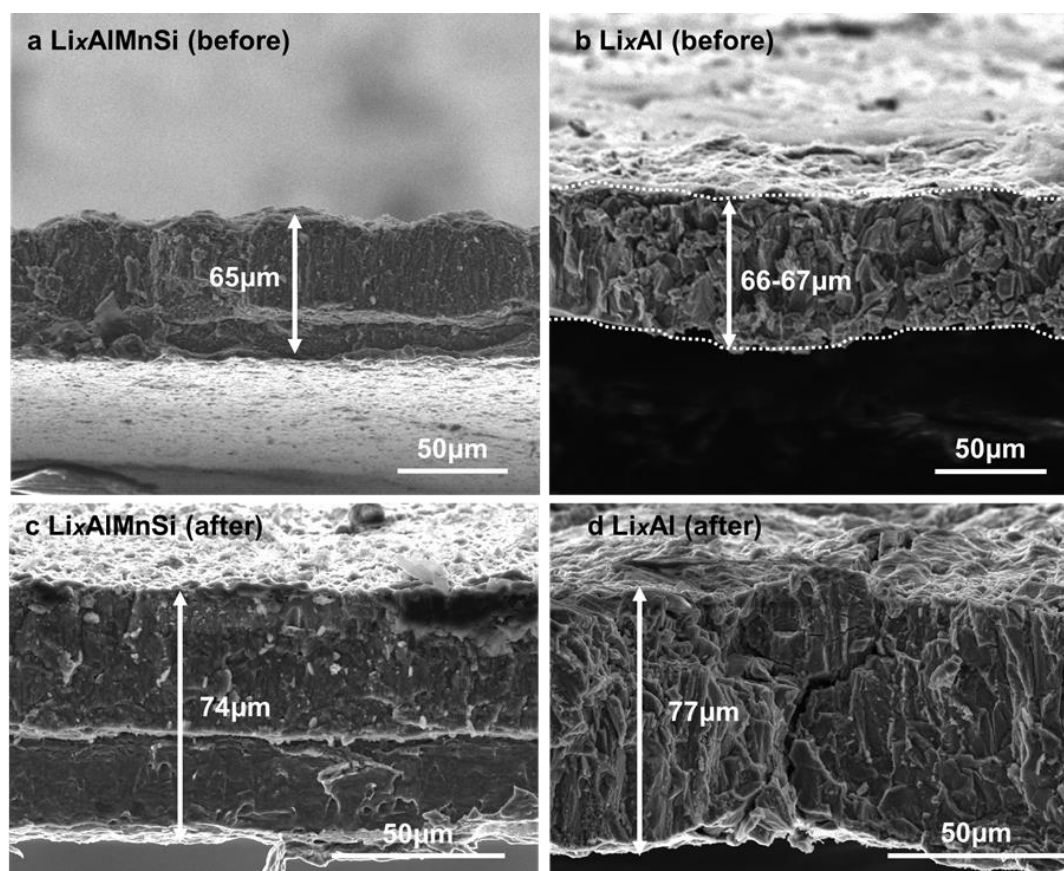


Figure S13. Cross-sectional SEM images of Li_xAl and Li_xAlMnSi foils before and after the electrochemical lithiation.

As revealed in Figure S13, large volume change still happens even for the Li_xAlMnSi anode, which intrinsically is originated from the nature of alloying anodes. However, although we acknowledge that the absolute volume expansion would not be restrained, in this study we find the apparent volume expansion seems to be mitigated. From the thickness comparison between the Li_xAlMnSi and Li_xAl , before the electrochemical lithiation process, Li_xAlMnSi (Figure S13a) and Li_xAl (Figure S13 b) anodes show 65 μm thick and 66-67 μm thick respectively from the original 40 μm thick after MP. Note that besides the average thickness that Li_xAl demonstrates 1-2 μm thicker than Li_xAlMnSi , some variation in their surface roughness is also observed. By measuring the thickness of 30 different points on the two anodes with micrometer, surface roughness of Li_xAl is determined to be 2.0 μm (Table S1), while that of Li_xAlMnSi is 1.4 μm (Table S2), which means apparent volume expansion is smaller and more uniform in AlMnSi during mechanical prelithiation. Further cross-sectional SEM analysis in Figure S13b reveals that the multiple damages, including cracks and pores, is attributed to the bigger apparent volume change of Li_xAl . In contrast, Li_xAlMnSi in Figure S13a exhibits a much more compact structure, which on the other hand implies smaller grain size and denser GB network that are induced by Zener pinning of metal alloy through adding impurity elements indeed alleviate the damage caused by the large volume change so as to reduce the apparent volume expansion.

Figure S13c and S13d respectively demonstrate the cross-sectional SEM images after electrochemically lithiating 2mAh cm^{-2} lithium into the above-obtained Li_xAl and Li_xAlMnSi . The thickness of Li_xAlMnSi anode grew to 74 μm , and the Li_xAl anode swelled to 77 μm , corresponding to 13.8% and 14.9% expansion rate, respectively. Although Li_xAlMnSi and Li_xAl foils have similar volume change ratio, they demonstrate totally different morphologies. As can be seen in Figure S13, evident cracks of Li_xAl anode penetrate the thickness direction (Figure S13d), and the electrode is damaged after lithiation, making the structure porous and fragile, which justifies well its larger apparent volume change. In a sharp contrast, the Li_xAlMnSi anode keeps tight structure without any cracks before (Figure S13a) and after electrochemical lithiation (Figure S13c) despite the same absolute volume change. That is to say, compared to Li_xAl , the Li_xAlMnSi anode have mitigated the fatal cracking consequences of volume expansion. We think it is attributed to the sufficient GB sliding system, by which the Li_xAlMnSi anode could easily release the residual stress during the lithiation and then avoid the growth of cracks, thus further alleviate concomitant side-effects caused by volume expansion.

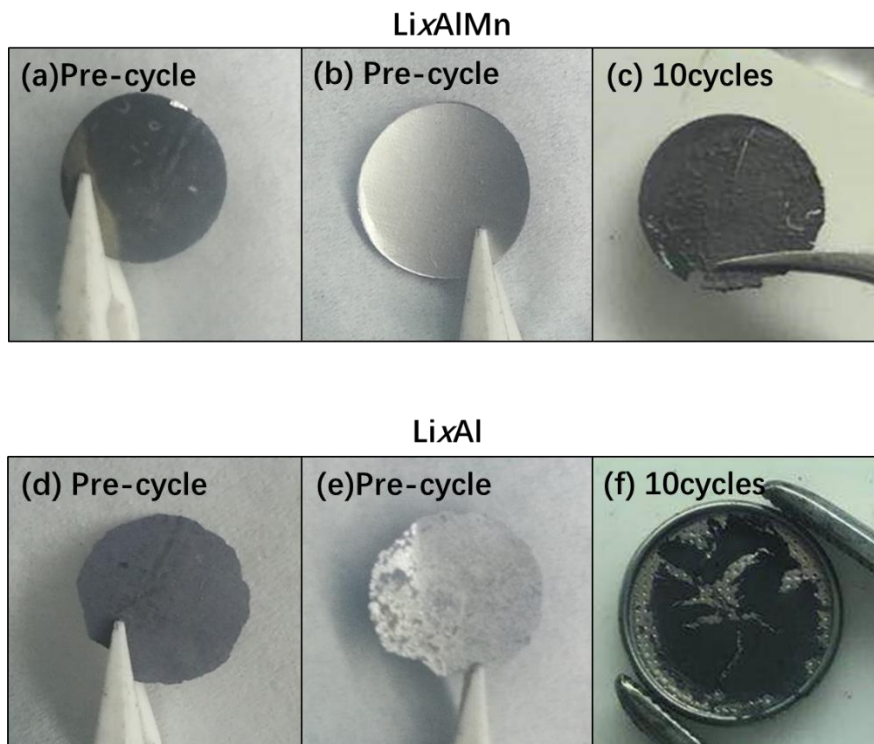


Figure S14. Optical photos of pre-cyclic Li_xAlMnSi (a and b) and Li_xAl (d and e), and Li_xAlMnSi (c) and Li_xAl(f) after 10 cycles in full-cells.

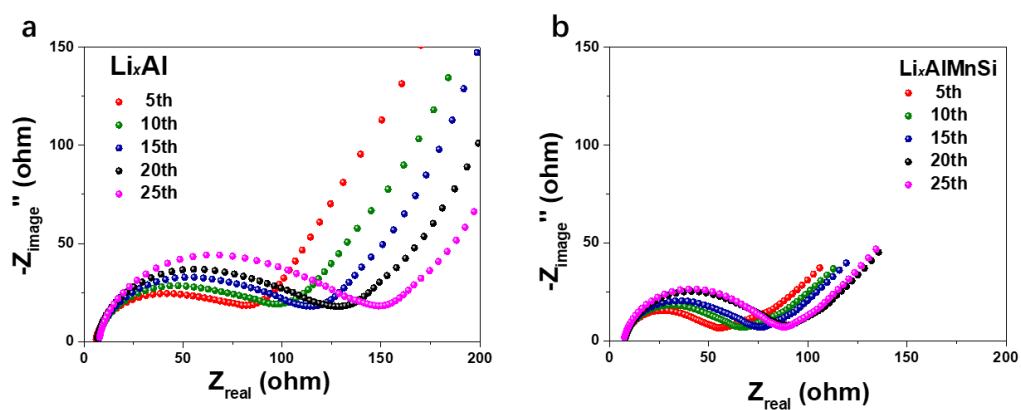


Figure S15. Interfacial resistance of LFP||Li_xAl(a) and LFP||Li_xAlMnSi (b) in the first 25 cycles.

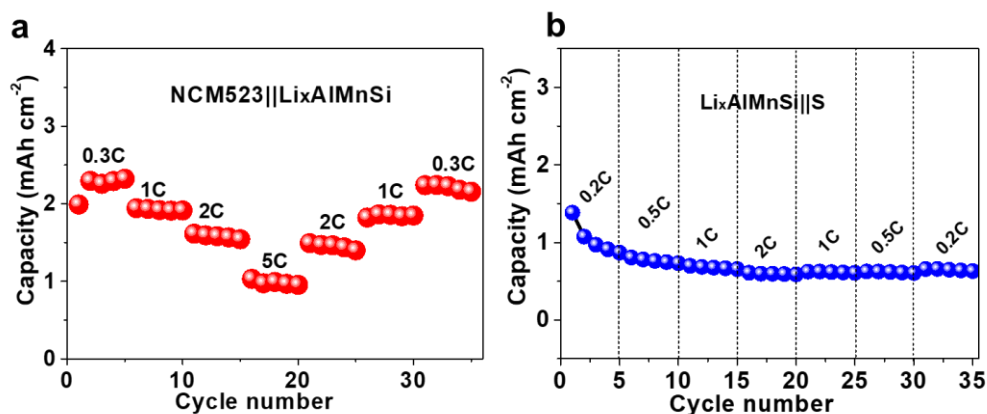


Figure S16. (a) Rate performance of NMC523||Li_xAlMnSi full cells and (b) Li_xAlMnSi||S batteries.

In addition, the rate performance of Li_xAlMnSi||S batteries is shown in Figure S16 (b), where the current density increased stepwise from 0.24 to 2.4 mA cm⁻². From Figure S16 (b), no significant capacity degradation occurs as current intensifies, indicating a decent rate performance of Li_xAlMnSi||S batteries. However, it is worth mentioning that Li_xAlMnSi is still chemically unstable against Li₂S_n, as indicated in Figure S17 (a), where the same ether-based electrolyte except for no LiNO₃ as additive was used in Li_xAlMnSi-S batteries. In contrast with Figure 6c (CE~99%), CE (CE=109%) in Figure S17 (a) deteriorates significantly when electrolyte consists of no LiNO₃, which is generally believed to form passivation layer so as to prevent the corrosion of Li₂S_n in Li-S batteries. Such speculation also gets verified by postmortem XPS examination in Figure S17 (c and d) and sulfur-containing species, including Li-S-O, Li-S composites, were detected on the cycled Li_xAlMnSi electrode surface. Therefore, it is reasonable to infer that Li_xAlMnSi anodes are still chemically reactive with Li₂S_n. Note that Li_xAlMnSi anodes are relatively more stable with Li₂S_n than Li metal anodes, where CE=125% (Figure S17 (b)) is observed.

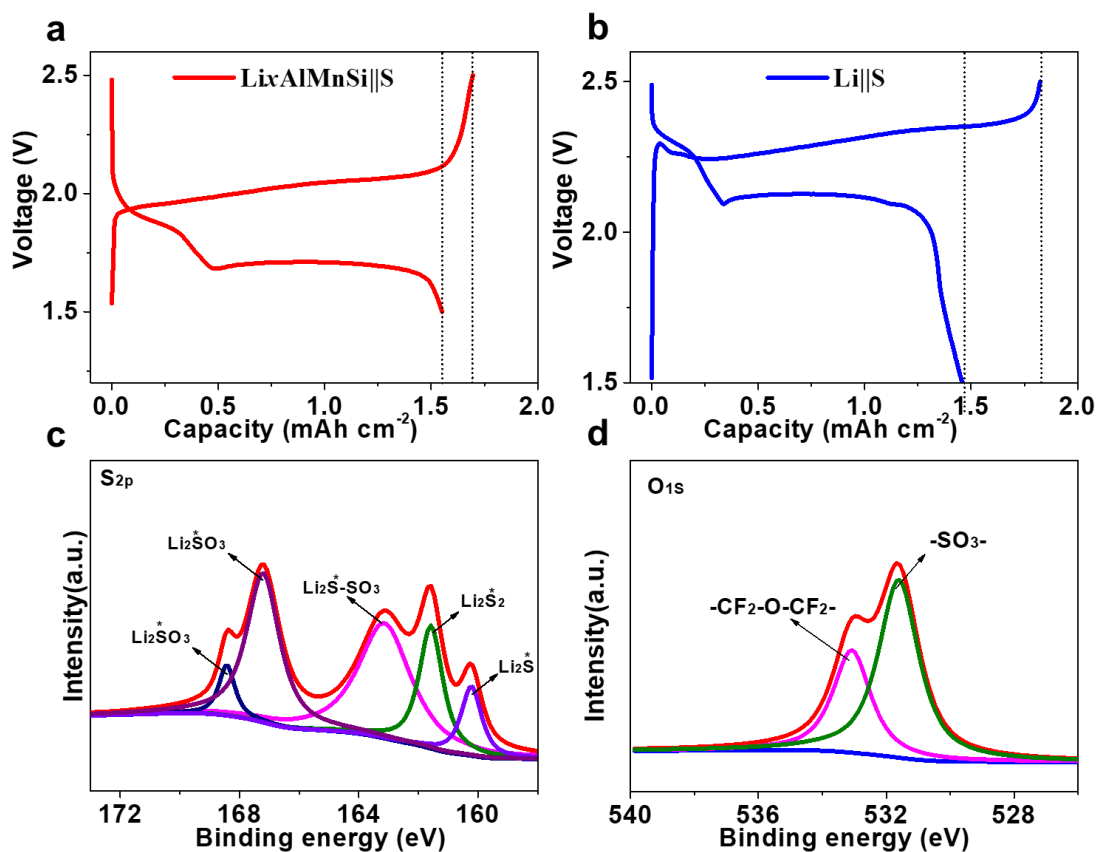


Figure S17. $\text{Li}_x\text{AlMnSi}||\text{S}$ (a) and $\text{Li}||\text{S}$ (b) batteries performance in the ether-based electrolyte consisting of 1 M LiTFSI in a solution of 1,3-Dioxolane (DOL) and 1,2-Dimethoxyethane (DME) (volume ratio: 1:1) without LiNO_3 additive. (c and d) XPS spectra of S2p and O1s after cycling of the $\text{Li}_x\text{AlMnSi}||\text{S}$ battery.

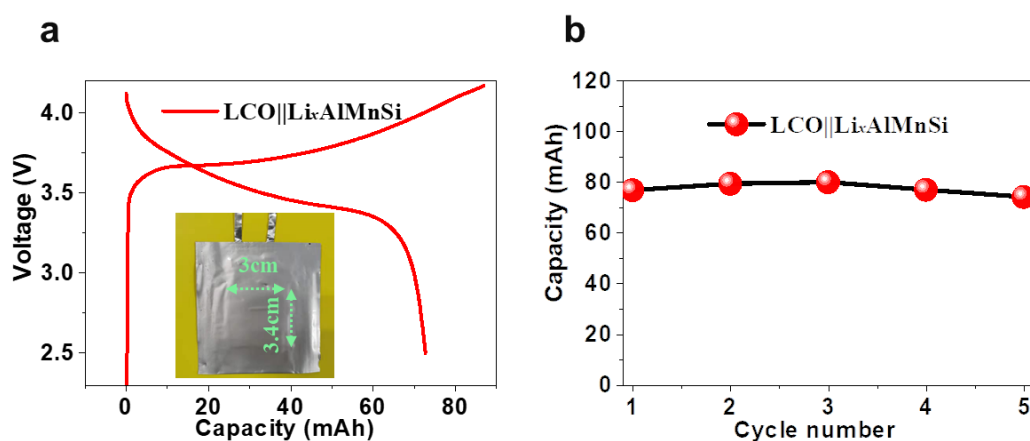


Figure S18. (a) Voltage curves of $\text{LCO} || \text{Li}_x\text{AlMnSi}$ pouch cell of the first cycle, inset picture is the photograph of the pouch cell. (b) Discharge capacity of the $\text{LCO} || \text{Li}_x\text{AlMnSi}$ pouch cell in the initial 5 cycles.

Table S1. Thickness (μm) measurement result of the Li_xAl sample.

Thickness (μm) of the foil					Average thickness	Standard Deviation	Total thickness
68.0	67.0	70.0	64.0	64.0	66.5 μm	2.0 μm	66.5 \pm 2.0 μm
67.0	70.0	63.0	67.0	68.0			
67.0	64.0	63.0	67.0	68.0			
68.0	65.0	64.0	64.0	67.0			
70.0	64.0	68.0	65.0	66.0			
68.0	65.0	67.0	63.0	68.0			

Table S2. Thickness (μm) measurement result of the Li_xAlMnSi sample.

Thickness (μm) of the foil					Average thickness	Standard Deviation	Total thickness
61.0	62.0	63.0	64.0	65.0	64.9 μm	1.4 μm	64.9 \pm 1.4 μm
67.0	63.0	65.0	66.0	65.0			
64.0	65.0	65.0	64.0	65.0			
69.0	63.0	64.0	66.0	67.0			
65.0	64.0	65.0	66.0	64.0			
65.0	66.0	66.0	65.0	67.0			

Table S3. Measured actual apparent thickness of all the samples.

Thickness (μm)	Al	AlMnSi	Li_xAl	Li_xAlMnSi
Total thickness (t_{total})	40	40	66.5	65.0
Reacted layer (t_{react})	--	--	66.5	50.6
Unreacted layer (t_{unrea})	--	--	0	14.4

Table S4. Thickness (μm) measurement result of the reacted layer of Li_xAlMnSi sample.

Thickness (μm) of the reacted layer					Average thickness	Standard Deviation	Reacted layer thickness t_{react}
47.5	51.0	50.0	50.0	52.0	50.6 μm	1.43 μm	50.6 \pm 1.43 μm
50.0	49.0	51.5	51.5	53.0			
52.0	50.0	49.0	49.0	50.0			
50.0	52.0	52.0	53.0	50.0			

Table S5. Lateral areal expansion of the two samples after MP.

Sample	Li _x AlMnSi	Li _x Al
Size (before MP)	4 cm × 3 cm	4 cm × 3 cm
Size (after MP)	4 cm × 3 cm	4.4 cm × 3.35 cm
Lateral areal expansion	0	22.8%
α	1	1.228

Table S6. Prelithiation degree at different mechanical pressure.

Mechanical Pressure	10MPa	15MPa	20MPa	30MPa
Li inventory (mAh cm ⁻²)	1.2	2.7	3.1	5.0

Table S7. Mole ratio calculation of the Al and Li inside the Li_xAlMnSi layer.

Component	Li	Al
Area (cm ²)	1	1
Thickness (cm)	0.0025	0.00256
Density (g/cm ³)	0.534	2.699
Mass (mg)	1.335	6.909
Mole (mmol)	0.1923	0.2560

Table S8. Calculation parameters of the grain size.

Parameters	K	λ (Å)	FWHM (°)	2 θ (°)	L (nm)
Values	0.94	1.54178	0.35	40.10	25

Table S9. Coloumbic efficiency of four LFP|| Li_xAlMnSi full-cells in the initial cycles.

CE(%)	1 st	2 nd	3 rd	4 th	5 th	6 th	7 th	8 th	9 th	10 th
1#	85.8	101.15	100.64	100.5	100.29	100.34	100.29	99.76	100.66	100.13
2#	87.71	100.93	100.53	100.31	100.16	100.24	100.11	100.15	100.12	100.05
3#	87.10	100.60	100.35	100.08	100.12	100.03	99.97	99.99	99.88	99.97
4#	86.10	100.40	100.12	99.93	99.85	99.81	99.80	99.91	99.85	99.91

Table S10. Parameters of the LCO || Li_xAlMnSi pouch cell.

Components	Thickness(μm)	Mass(mg)	Volume(μL)	Capacity(mAh)
LiCoO ₂	290	630	--	72.7
Li _x AlMnSi	140	272	--	--
Separator	15	32.5	--	--
Electrolyte	--	288	240	--

REFERENCES

- (1) Kasnatscheew, J.; Evertz, M.; Streipert, B.; Wagner, R.; Nowak, S.; Cekic Laskovic, I.; Winter, M. *The Journal of Physical Chemistry C*.**2017**, *121*, 1521-1529.
- (2) Kasnatscheew, J.; Evertz, M.; Streipert, B.; Wagner, R.; Klopsch, R.; Vortmann, B.; Hahn, H.; Nowak, S.; Amereller, M.; Gentschev, A. C.; Lamp, P.; Winter, M. *Phys Chem Chem Phys*.**2016**, *18*, 3956-65.
- (3) Zheng, Y.; Wang, Y.; Lu, Y.; Hu, Y.-S.; Li, J. *Nano Energy*.**2017**, *39*, 489-498.
- (4) Zheng, Y.; Lu, Y.; Qi, X.; Wang, Y.; Mu, L.; Li, Y.; Ma, Q.; Li, J.; Hu, Y.-S. *Energy Storage Materials*.**2019**, *18*, 269-279.